622

Implementation of an ocean mixed layer model in IFS

Y. Takaya[1,2], F. Vitart[1], G. Balsamo[1], M. Balmaseda[1], M. Leutbecher[1], F. Molteni[1]

Research Department

[1]European Centre for Medium-Range Weather Forecasts, Reading, UK
[2]Japan Meteorological Agency, Tokyo, Japan

March 2010

Abstract

An ocean mixed layer model has been implemented in the ECMWF Integrated Forecasting System (IFS) in order to have a better representation of the atmosphere-upper ocean coupled processes in the ECMWF medium-range forecasts. The ocean mixed layer model uses a non-local K profile parameterization (KPP; Large et al. 1994). This model is a one-dimensional column model with high vertical resolution near the surface to simulate the diurnal thermal variations in the upper ocean. Its simplified dynamics makes it cheaper than a full ocean general circulation model and its implementation in IFS allows the atmosphere-ocean coupled model to run much more efficiently than using a coupler.

The atmosphere-ocean mixed layer coupled model has been assessed by computing the skill of ensemble 10-day and monthly forecasts. Preliminary verifications indicate that the overall skill scores of the ensemble forecast are comparable to the skill scores of the current operational system. However, the ocean mixed-layer model has a positive impact on the prediction of the Madden Julian Oscillation and the Indian monsoon. The ocean mixed-layer model has also an impact on the intensity of tropical cyclones. The diurnal variability of SST which is important for future applications such as data assimilation with coupled models has also been evaluated.

1   Introduction

The upper 2.5 m ocean has about the same heat capacity as the entire column of the atmosphere. The near-surface ocean absorbs more than 60 % of the solar radiation and has large diurnal variability up to several degrees in clear sky and calm wind conditions. This indicates that a huge amount of heat is exchanged at the ocean surface between the atmosphere and the ocean on a diurnal time scale. The diurnal variability of SST has a significant influence on heat and radiation exchanges at the ocean surface (Fairall et al. 1996; Zeng and Dickinson 1998; Brunke et al. 2008). Therefore a better representation of the upper ocean is expected to improve the simulation of surface fluxes in numerical weather and climate models. Furthermore, the improved diurnal variability of surface fluxes contributes to a better representation of the atmospheric variability.

At longer forecast range, the upper ocean interacts with various aspects of the atmospheric variability from diurnal to intraseasonal time scales (Webster et al. 1996; Slingo et al. 2003; Kawai and Wada 2007). In particular, the Madden-Julian Oscillation (MJO; Madden and Julian 1994; Zhang 2005) has a coherent signal in both the atmosphere and ocean implying that the air-sea interaction plays a role in its mechanism (Hendon and Glick 1997; Lau and Sui 1997; Jones et al. 1998). The impacts of the air-sea interaction on the MJO have been investigated for a long time (e.g., Flatau et al. 1997; Waliser et al. 1999; Maloney and Sobel 2004). The ocean-atmosphere coupling improves the propagation speed, structure and amplitude of the MJO in the numerical weather prediction (NWP) models (e.g., Sperber et al. 2005; Zheng et al. 2004, Maloney and Sobel 2004, Inness and Slingo 2003). Recently, Woolnough et al. (2007) and Vitart et al. (2007) have demonstrated that the skill of the ECMWF monthly forecasts to predict the evolution of the MJO is improved by coupling IFS to an ocean mixed layer model via the OASIS2 coupler.

Furthermore, the remote influence of the MJO is of great interest because of its implication on the potential predictability on monthly time scale (Donald et al. 2006; Ferranti et al. 1990; Hendon et al. 2000; Jones et al. 2004; Knutson and Weickmann 1987; Vitart and Molteni 2009a). These studies demonstrated the MJO has a remote impact on the extratropic circulation through teleconnections. In addition, the MJO modulates several aspects of atmospheric variability. For instance, the MJO modulates the sub-seasonal activity in the Asian monsoon (Yasunari 1979; Lau and Chan 1986; Webster et al. 1998; Lawrence and Webster 2002), North American monsoon (Maloney and Esbensen 2003) and African monsoon (Matthews 2004; Maloney and Shaman 2008). The MJO also modulates tropical cyclone activity (Camargo et al. 2009; Kim et al. 2008; Liebmann et al. 1994; Nakazawa 1986; Vitart 2009) and triggers and/or enforces ENSO events (Kessler and

Kleeman 2000; Bergman et al. 2001; Marchall et al. 2009). Therefore, improving the prediction of the MJO is likely to lead to improved forecasts of extratropical circulation, monsoon and tropical cyclone variability on monthly to seasonal time scales.

The western North Pacific and Indian Ocean in boreal summer are other areas where the ocean-atmosphere coupling plays a key role. In these regions, the convection is active and the oceanic mixed layer depth is shallow in boreal summer. These factors make the SST to respond quickly to atmospheric forcing. Local SSTs and precipitation are anti-correlated with a 5-10 days lag (Arakawa and Kitoh, 1997). A better representation of the ocean-atmosphere interaction is expected to help reproduce the realistic relationship between precipitation and SST. A study with multiple uncoupled atmospheric models showed that the uncoupled models failed to reproduce this relationship (Wang et al. 2005) and that ocean coupling was needed to simulate the relationship properly (Inness and Slingo 2003; Kobayashi et al. 2005). Therefore, ocean coupling is likely to impact the atmospheric and oceanic variability in the short and medium-range time scales.

Following these meteorological studies and the recommendations made at the ECMWF workshop on the role of the upper ocean in medium and extended range forecasting in 2002 and the ECMWF workshop on ocean-atmosphere interactions in 2008, we implemented an ocean mixed layer model in IFS. The ocean mixed layer model has been implemented as part of the physics in IFS and it uses the same horizontal grid as the atmospheric model grid. This implementation method and the simplified dynamics enable us to run the ocean mixed layer-atmosphere coupled model at a reasonable computational cost.

The technical implementation details and model configurations will be described in the next section. In section 3, the verification of EPS forecasts with the ocean mixed-layer model will be shown. In Section 3, the impact of the ocean mixed-layer model on the SST variability, Indian monsoon rainfall, MJO and tropical cyclone forecasts will also be discussed. Section 4 will assess the SST diurnal cycle. Finally, Section 5 will present a summary of this report.

2 Implementation

2.1 Model configuration

The ocean mixed layer model is the same version of the KPP model as in Woolnough et al. (2007), which follows the formulation of Large et al. (1994). The KPP scheme is widely used in many ocean models. For example, the scheme is used in the MOM3 ocean model, which is an operational ocean model in the NCEP coupled model (Saha et al. 2006). In this section, only the modified aspects from Large et al. (1994) or Woolnough et al. (2007) are described.

The water type for a solar radiation parameterization has been changed to the Jerlov water type I (Jerlov, 1976), instead of the water type Ib in Woolnough et al (2007). The water type I is a more realistic choice for the global ocean, and is commonly used in ocean general circulation models (OGCMs). This change is intended to deepen the ocean mixed layer depth in summer, which tends to be too shallow in many ocean models, and reduce warm SST bias in the summer hemisphere. The diurnal amplitude of SST is affected by this change, since absorption of solar radiation is influenced by the water type (e.g., Shinoda 2005).

The double-diffusion mixing in the KPP scheme has been deactivated. With the double-diffusion switched on, the model develops relatively large cool SST bias in winter time at mid-latitudes (30 °N and 30 °S) west of continents. The double-diffusion mixing was not applied in Woolnough et al. (2007) and Vitart et al. (2007) either. The double-diffusion formulation proposed in Danabasoglu et al. (2006) was tested, but the error was not alleviated. The cause of the cold bias has not been investigated in detail. It may not be caused by the double
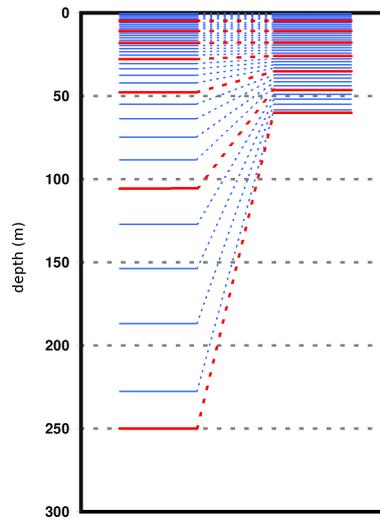
Figure 1: Schematic figure of the stretched vertical grid. The left (right) column shows vertical levels for 250-m (60-m) bathymetry.

diffusion itself. For instance, it could be caused by an imbalance between the salinity and temperature fields of the initial conditions from the ECMWF ocean analysis (Balmaseda et al 2008) and the KPP scheme.

The viscosity and diffusivity of internal gravity waves have been increased to 1.5×10^{-4} and 1.5×10^{-5}, respectively, and the critical bulk Richardson number is set to 0.4[1]. The net effect of these changes is to deepen the mixed layer, reducing the warm SST bias in summer, although the impact of these changes in the 10-day forecasts of SST is relatively minor.

Changes have been made as to take the bathymetry into account, in contrast to a uniform bathymetry (200 m) in Woolnough et al. (2007) and Vitart et al. (2007). In the current setting, the largest depth is 250 m to cover the midlatitude mixed layer depth (de Boyer et al. 2004). With variable ocean depth, the original stretched grid refinement (Large et al. 1994; Bernie et al. 2006) produces variable layer thickness near the surface, which can affect the diurnal SST variability in the KPP model (Bernie et al. 2006). A new stretched vertical grid refinement is introduced to guarantee uniform thickness of the first level. In this formulation, the level depth is computed with the following expression:

$$d_n = an + b \left(\frac{n-1}{M-1} \right)^c + d \left(\frac{n-1}{M-1} \right)^e \qquad (n = 1, 2, ..., M) \qquad (1)$$

where $M = 35$ is the number of layers, $a = 1.0$ m, $b = D - aM - d$ m, $c = 8.0$, $d = 20.0$ m and $e = 2.0$ are parameters, and D is the lowest level of the ocean mixed layer model. The distribution of vertical levels given by the new formulation is illustrated schematically in Figure 1.

In this configuration, the thickness of the first level has been chosen to be 1 m, following the findings of Bernie et al. (2005), who noted that the thickness of the top level must be of the order of 1 m to capture the diurnal SST variability with their KPP model. They also reported that further increase of the vertical resolution to 0.5 m had a relatively minor impact on the diurnal SST amplitude in the KPP model.

The coupling domain is $40\,°$N to $40\,°$S [2], since relatively large SST errors can develop at higher latitudes. Within the halo ($40\,°$N-$30\,°$N, $40\,°$S-$30\,°$S), SSTs from predicted by the KPP model are smoothly blended with

---

[1]In Woolnough et al. (2007), the viscosity and diffusivity of internal gravity waves and the critical Richardson number are 1.0×10^{-4}, 1.0×10^{-5} and 0.3, respectively

[2]In Woolnough et al. (2007), the coupled domain is $44\,°$N to $44\,°$S

prescribed SSTs before being passed to the atmospheric model, and outside the coupling domain, the SSTs seen by the atmosphere model are fully prescribed. The prescribed SSTs are persisted SST anomalies, estimated in the same way as in the first 10-day forecasts of ECMWF EPS. The ocean mixed layer model is coupled at every time-step, by receiving surface fluxes from the atmospheric model and passing updated SST to the atmospheric model.

Initial ocean conditions are produced by interpolating the ECMWF operational ocean analysis (Balmaseda et al. 2008). The nearest four points are used to interpolate with an inverse distance weight. The ECMWF ocean analysis has coarser resolution than the SST used to force the current EPS. In order to retain the high-resolution SST information, the ocean temperature of the initial conditions is changed above the mixed layer, as to match the high resolution SST fields used in the EPS. The mixed layer depth is diagnosed from the ocean analysis as the depth where temperature departs more than 0.5 degrees from its surface values. With this correction, the initial SST fields are identical to the prescribed SST fields in the EPS.

Preliminary integrations with the KPP model displayed an unrealistic behaviour in the ocean currents. The ocean currents in the one-dimensional model are basically governed by the one-dimensional dynamics (Ekman flow), without pressure gradient terms, causing the ocean currents to rotate with the inertial frequency. In reality however, the ocean currents in the extratropics are roughly geostrophically balanced. This deficiency of one dimensional models has been identified for simulations of the atmospheric boundary layer (e.g., Egger and Schmid, 1988), but not so for atmosphere-ocean mixed layer coupled models.

Therefore, the treatment of the velocity in the mixed layer model needs additional care. Here, the currents from the ocean analysis have been decomposed into slow and fast varying flow. The later is assumed to be mainly the Ekman flow, and can possibly be simulated by the one-dimensional KPP model. This approach is similar to the method proposed in Egger and Schmid (1988) for simulations of the atmospheric boundary layer (see also Taylor (1989), Egger and Schmid (1989)). The total velocity follows the equations:

$$\frac{\partial U}{\partial t} = -\frac{1}{\rho}\frac{\partial P}{\partial x} + fV + \frac{\partial}{\partial z}\left(K(U,V,T,S,t)\frac{\partial U}{\partial z}\right) \tag{2}$$

$$\frac{\partial V}{\partial t} = -\frac{1}{\rho}\frac{\partial P}{\partial y} - fU + \frac{\partial}{\partial z}\left(K(U,V,T,S,t)\frac{\partial V}{\partial z}\right) \tag{3}$$

where U and V are zonal and meridional velocity, ρ is the water density, K is a viscosity function and f is the Coriolis parameter. Decomposing geostrophic and ageostrophic (Ekman) flow components, the equations are written as

$$\frac{\partial(U_g+U_e)}{\partial t} = -\frac{1}{\rho}\frac{\partial(P_g+P_e)}{\partial x} + f(V_g+V_e) + \frac{\partial}{\partial z}\left(K(U_g+U_e,V_g+V_e,T,S,t)\frac{\partial(U_g+U_e)}{\partial z}\right) \tag{4}$$

$$\frac{\partial(V_g+V_e)}{\partial t} = -\frac{1}{\rho}\frac{\partial(P_g+P_e)}{\partial y} - f(U_g+U_e) + \frac{\partial}{\partial z}\left(K(U_g+U_e,V_g+V_e,T,S,t)\frac{\partial(V_g+V_e)}{\partial z}\right) \tag{5}$$

where subscripts g and e indicate geostrophic and non-geostophic flow components. Next we assume that the geostrophic component is balanced and do not evolve in short integrations of about 10 days. We estimate the geostrophic component as the 10-day averaged ocean currents from the ocean analysis. In addition we assume that the pressure gradient terms of the non-geostrophic part can be neglected, and that the viscosity function K can be computed by using a superposition of a geostrophic flow and non-geostrophic flow[3]. Then the results are given as:

$$\frac{\partial U_e}{\partial t} = fV_e + \frac{\partial}{\partial z}\left(K(U_g+U_e,V_g+V_e,T,S,t)\frac{\partial U_e}{\partial z}\right) \tag{6}$$

---

[3]Strictly speaking, we need an approximation, $\frac{\partial}{\partial z}\left(K(U_g,V_g,T,S,t)\frac{\partial U_e}{\partial z}\right) \sim \frac{\partial}{\partial z}\left(K(U_g+U_e,V_g+V_e,T,S,t)\frac{\partial U_g}{\partial z}\right)$. Since the viscosity function is non-linear, this relation may not hold as a good approximation.
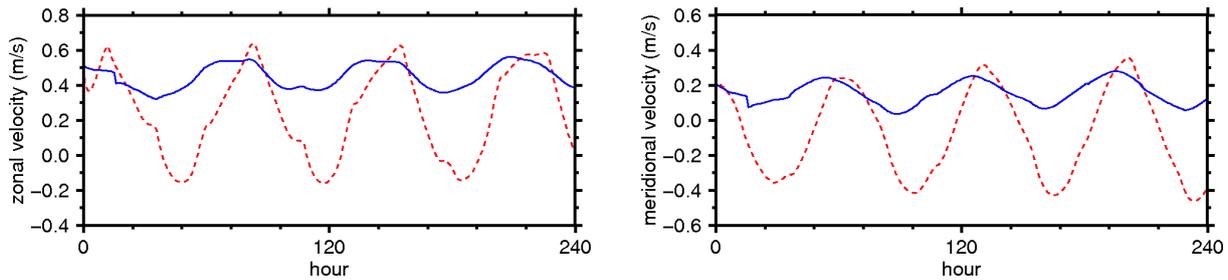
Figure 2: Simulated ocean currents at 18 m depth at 10°N, 55°E: (left) zonal component, (right) meridional component. Solid and dashed lines indicate current with and without the geostrophic current decomposition, respectively. The initial date is 11/07/1993.

$$\frac{\partial V_e}{\partial t} = -fU_e + \frac{\partial}{\partial z}\left(K(U_g + U_e, V_g + V_e, T, S, t)\frac{\partial V_e}{\partial z}\right) \tag{7}$$

$$\tau_e = \tau - \tau_g \tag{8}$$

where τ, τ_g and τ_e represent the total surface momentum flux, the previous 10-day average value, and the departure, respectively. The equations are similar to the original equations without the pressure gradient term, but the equations above describe the deviation flow from the nearly balanced flow. This may be valid only for short-term integrations of a few days. Figure 2 shows an example of time-series of ocean current away from the equator. Without the decomposition, the ocean current including a geostrophic balanced component starts to rotate with the inertial frequency from the beginning of the integration. With the decomposition, the spurious rotation of the flow is less dominant.

Regarding the computational cost, the coupling of this model increases the total CPU time of IFS by about 7 %. The one-dimensional model has good scalability because each ocean grid can be computed in parallel, and can be run at higher resolution. In fact the model runs at T1279L91 with reasonable computational resources. The cost can be reduced if the ocean model is called at a longer time step. It is worth noting that the KPP model can have much higher horizontal resolution than the general coupled models for monthly and seasonal forecasts (Vitart et al. 2008).

2.2 Code validation with an off-line simulation

The KPP scheme has been rewritten following IFS coding rules and parallelised with OpenMP and MPI. It has been tested in an off-line simulation using the TOGA-COARE observations in the western Pacific. Bernie et al. (2005) demonstrated that the KPP model reproduces realistic diurnal variability of subsurface temperature with the TOGA-COARE observations. Shinoda and Hendon (1998) also examined the temperature variation during the TOGA-COARE period with the KPP model. Here, we confirm the performance of the implemented KPP model by comparing our result to theirs.

The off-line model is forced by surface fluxes computed from the IMET observations on the WHOI mooring buoy at 1° 45′ S, 156° E during the COARE period (Weller and Anderson 1996). Initial conditions of ocean subsurface fields on the 1 November 1995 are given by the moored buoy observations. The model is integrated for 3 months. In this simulation, the geostrophic flow decomposition described in the previous section is not applied since the Coriolis force is negligible near the equator. It should be noted that no relaxation of SST or other fields is applied in this simulation. Figure 3 displays the resulting subsurface temperature and sub-skin SST. The model reproduces the strong mixing due to convection after sunset and the variability of a diurnal thermocline (mixed layer depth). A modest warm bias error is seen in the later part of the integration. This behaviour has also been reported in Shinoda and Hendon (1998) and Bernie et al. (2006). Shinoda and Hendon

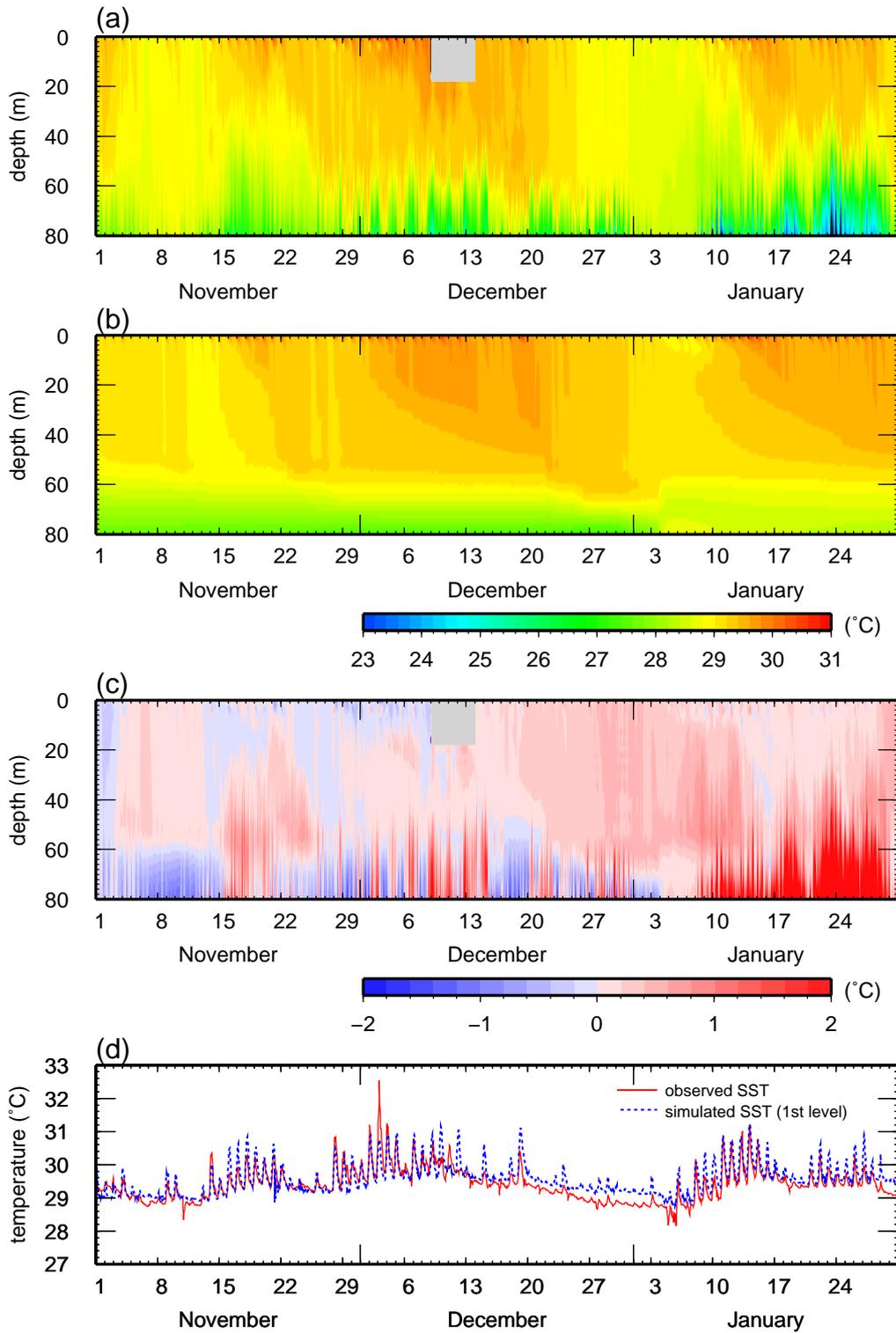*Figure 3: Simulated and observed subsurface temperature and SST at 1° 45'N, 156°E during the TOGA-COARE period from 1 November to 31 January: (a) observed subsurface temperature (b) simulated subsurface temperature with KPP model, (c) difference of subsurface temperature between the observation and the simulation, (d) SST time-series.*

(1998) attributed this error to errors in the surface heat fluxes and/or neglected horizontal advection, and/or other deficiencies of the one-dimensional model. A previous study of the heat budget had shown that an advection takes heat from the TOGA-COARE area around the end of December (Feng et al. 2002). The simulation shows a similar variability to the result in Bernie et al. (2006). Thus, we conclude that the implemented model works properly, and reproduces the subsurface temperature variability in the off-line simulation.

3   Results

3.1   Case study

In a medium-range time scale, the KPP coupled model is expected to simulate the coherent interaction between the ocean and the atmosphere as observed for instance during an MJO event. A case study of a 10-day forecast starting from 15 October 2008 is presented in this section to demonstrate the impact of the KPP coupled model on the ocean variability. The first integration is carried out with the KPP model (KPP). The second integration has been performed with IFS forced by persisted SST anomalies and with a skin layer scheme (ZB05; Zeng and Beljaars 2005), which represents the diurnal variability of SST. The last integration is a control integration (CTRL) with IFS forced with persisted SST anomalies but without KPP and ZB05. In this control experiment, there is no diurnal variability of SST.

In the middle of October 2008, an MJO event started to propagate from the Indian Ocean towards the maritime continent. Figure 4 shows a Hovmöller diagram of NOAA interpolated outgoing longwave radiation averaged within $10\,°N–10\,°S$ (Liebmann and Smith 1996) in October 2008. An active convection phase (low OLR) was observed from the middle to the end of October across $60–150\,°E$. This case shows a typical MJO eastward propagation and a coherent relationship between the atmospheric and oceanic variability (Matthews 2004; Sperber 2003).

Figure 5 shows the change of SST at day 10 from the initial conditions. The KPP model captures the spatial distribution of the SST change quite well without any relaxation or nudging. The seasonal cycle of SST is reproduced by the KPP model. Furthermore, the SST warming off the northwest coast of Australia and in the South Pacific Convergence Zone (SPCZ) is in good agreement with the SST analysis. The SST cooling off the east coast of the horn of Africa is also in good agreement with the analysis. The warming near the maritime continent and the SPCZ is a typical time evolution ahead of the active convection phase of MJOs. The cooling in the eastern Indian Ocean is also consistent with the MJO propagation. On the other hand, the persisted SST anomalies, which are used in the current operational EPS, have only a climatological seasonal cycle of SST (Figure 5b). Woolnough et al. (2007) also demonstrated that the KPP model captures the SST variability associated with an MJO event reasonably well. The tropical instability waves which are visible in the analysis are not simulated in both the CTRL and KPP experiments. The skill of the KPP coupled model to forecast SSTs will be evaluated in section 3.2.

The diurnal variability of skin SST is diagnosed using a Diurnal SST Amplitude (DSA), which is defined as the difference between the maximum and minimum SSTs during a day (00 LMT to 24 LMT). The DSA is computed from hourly output of the IFS integrations. Figure 6 shows an example of DSA in 10-day forecasts. Both the ZB05 and the KPP model can represent the diurnal variability of SST. The figures displays a large DSA near the maritime continent. Large DSA is often preceeded by an active phase of the MJO (e.g., Lau and Sui 1997; Bellenger and Duvel 2009). Section 3.7 will show more detailed diagnostics of the DSA in the KPP model and the skin layer scheme.

Figure 7 shows the impact of the diurnal SST variability on precipitation. Both KPP and ZB05 experiments
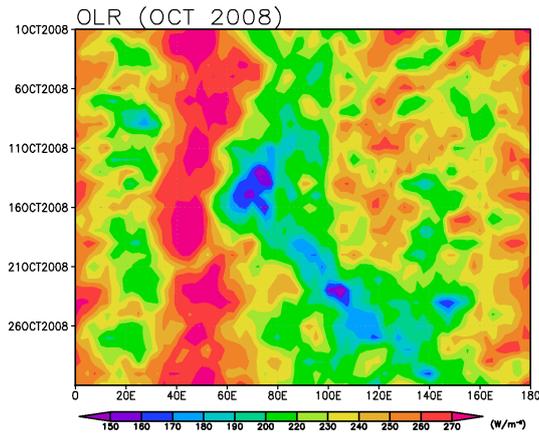
Figure 4: Hovmöller diagram of observed outgoing longwave radiation in October 2008.
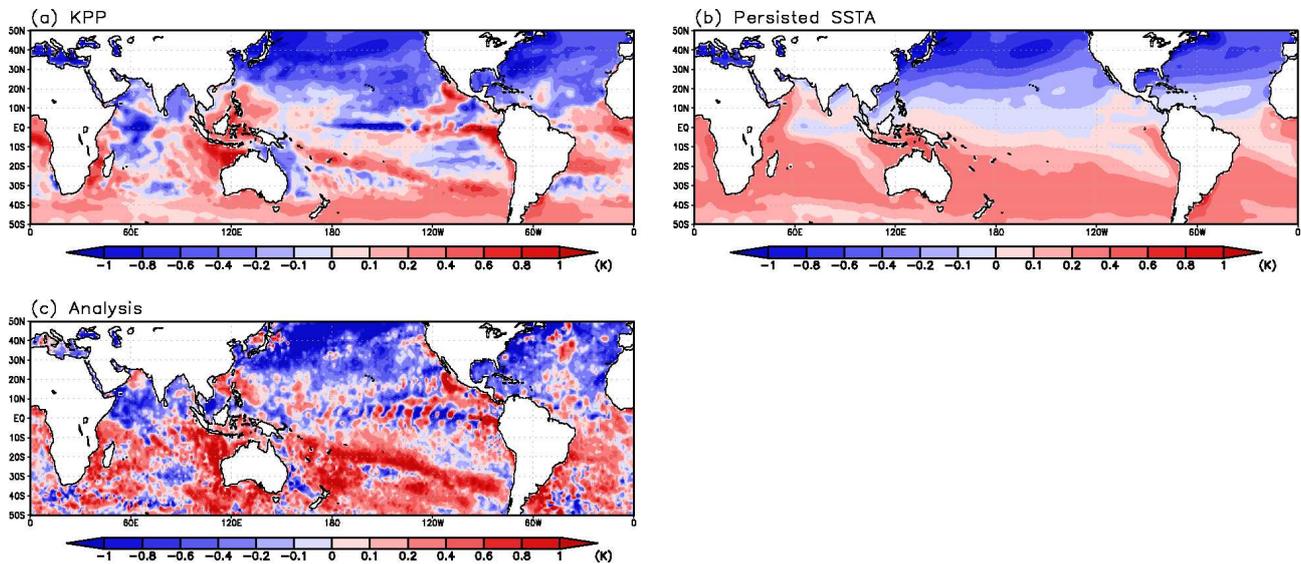

Figure 5: SST change (day10−day0) in the forecasts starting from 15th of October, 2008: (a) 5-m SST in the KPP model (KPP), (b) persisted SST anomaly (CTRL), (c) SST analysis.

show enhanced precipitation ahead of the MJO (over the maritime continent and the western North Pacific), and suppressed precipitation behind the MJO (over the central Indian Ocean). This result suggests that the MJO propagation is enforced by the diurnal SST variability. Woolnough et al. (2007) noted that a part of the MJO forecast improvements observed when using an ocean mixed layer model were due to the simulation of the SST diurnal cycle. Vitart and Molteni (2009b) reported that MJOs in IFS tend to stay longer in the Indian Ocean. Therefore simulating the diurnal SST variability seems to improve the MJO propagation in the Indian Ocean (e.g., Vitart et al. 2007).

3.2 SST validation

In order to evaluate the basic performances of the KPP coupled model, a series of 10-day 5-member ensemble integrations at a T255L62 resolution has been performed. The IFS version is the cycle 35r2[4]. The initial

---

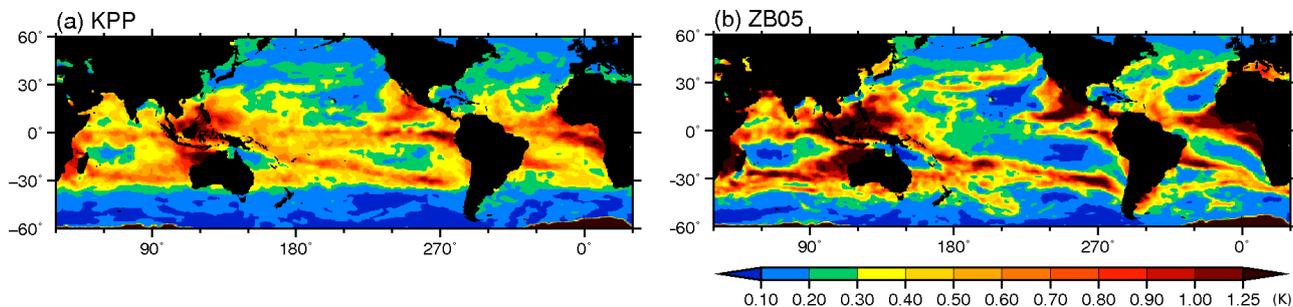[4]A bug in the McICA radiation scheme is fixed in the experiments.

Figure 6: Simulated diurnal SST amplitude during 10-day forecasts starting from 15th of October, 2008: (a) KPP model (b) ZB05 scheme.
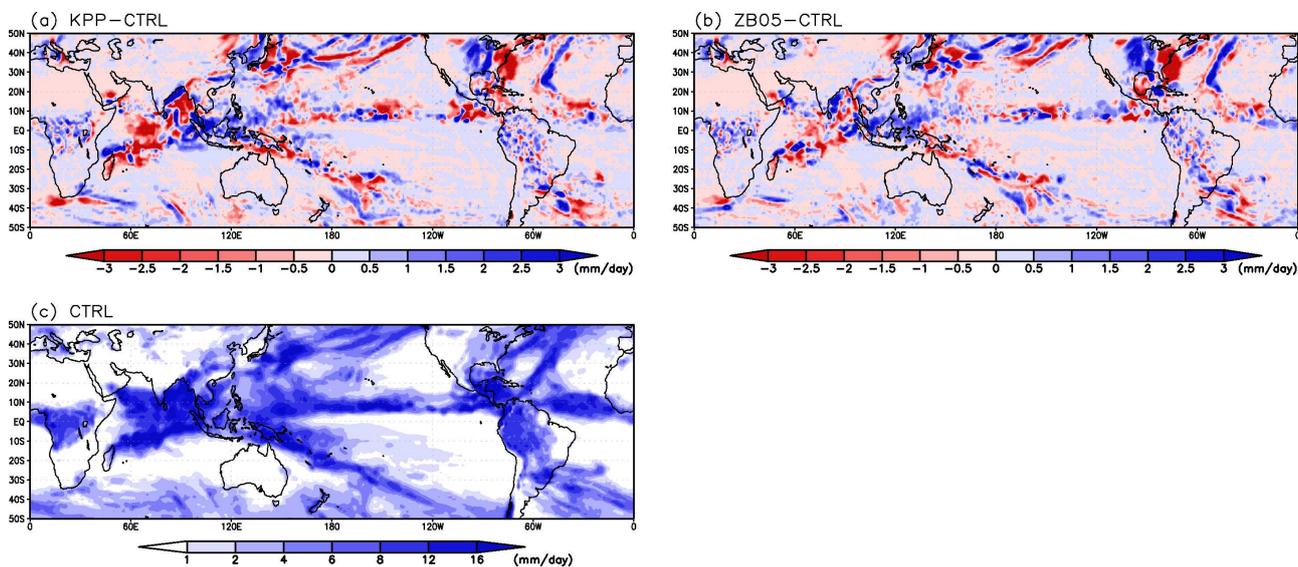

Figure 7: Simulated precipitation during 10-day forecasts starting the 15th of October 2008: (a) difference between KPP and CTRL, (b) difference between ZB05 and CTRL, (c) CTRL

dates are the 1st and 16th of January (July) 1990 to 2007 for boreal winter (summer) cases. The atmospheric initial conditions are provided by the ERA-Interim re-analysis (Simmons et al. 2007) and the oceanic initial conditions are provided by the ECMWF operational ocean analysis (Balmaseda et al. 2008). The deterministic forecast scores were computed from the ensemble mean.

Figure 8a shows the near-surface temperature bias after 10 days (00Z and 12Z) for the winter cases. The temperatures at the fifth level (~ 5 m) of the mixed layer model are compared to the bulk SST analysis (NCEP OI SST). The SST bias is about a few tenth of a degree in the coupled domain. It is worth noting that the bias has been improved with the modified configuration compared to the original configuration used in Woolnough et al. (2005) and Vitart et al. (2007).

For the root mean square error (RMSE), the KPP model displays relatively small errors in the subtropical region. However, the RMSE is large in the eastern equatorial Pacific since the KPP model is unable to simulate ENSO dynamics and cannot maintain SST anomalies in this region. This error is less striking in the correlation scores because of the strong interannual variability in this region. The RMSE is also large in the tropical Pacific along $10\,^\circ$N in January and the tropical Indian Ocean along $10\,^\circ$S in July. The origin of these errors should be further investigated.

In order to compare the skill of the coupled model to predict SST, the RMSE difference between the control and KPP experiments normalised by the RMSE of the control experiment has been computed along with the difference of correlations between the control and the KPP experiment (Figure 9). It should be noted that the 5 ensemble members of the control experiment use the same persisted SST field as in the operational EPS. Comparisons for both seasons show overall positive impacts (warm colours) when using the KPP model in the summer hemisphere. The improvement is particularly large (more than 20 %) in the western North Pacific in the boreal summer and in the SPCZ in austral summer. This may be due to the fact that the evolution of the SST is influenced by the strong air-sea interaction which can be simulated by the KPP model. However there are some degradations in the winter hemisphere and equatorial regions when using the KPP model. For the eastern equatorial Pacific, an OGCM has better skill at predicting SST after 1 month (not shown). It could be possible to nest the ocean mixed layer model in a lower-resolution OGCM. Future research will investigate this possibility.

Brenner (1996) investigated the potential use of an ocean mixed layer-atmosphere coupled model for medium- to extended-range forecasts with the NCEP model. There were some limitations at the time of this study: no ocean analysis was available for oceanic initial conditions, the atmospheric model had relatively low resolution, and a limited number of cases were verified. Despite these limitations, the study demonstrated that the coupled model can improve the SST forecast particularly in the summer hemisphere. Brenner (1996) reported that the coupled model can reduce the RMSE by 10–15 % compared to the uncoupled forecast (persisted SST anomalies). Our results indicate a similar order of improvements in the summer hemisphere (Figure 9).

3.3   EPS verification

The skill of the summer and winter EPS forecasts described in the previous section has been assessed. Figure 10 displays the 850-hPa temperature forecast scores for the northern extratropics, southern extratropics, and tropics in boreal winter. The differences between the coupled and uncoupled forecasts are not statistically significant. Figure 11 shows the 500-hPa geopotential height forecast scores. Again, there is no significant difference between the skill scores. Similarly, Figures 12 and 13, which show the scores in boreal summer, suggest that there is no significant improvement when using the KPP model.

We also conducted a series of monthly forecast integrations with a recent IFS cycle (cycle 35r2) in order to evaluate the impact of the KPP model on the probabilistic forecast skill scores. Fifteen-member ensemble
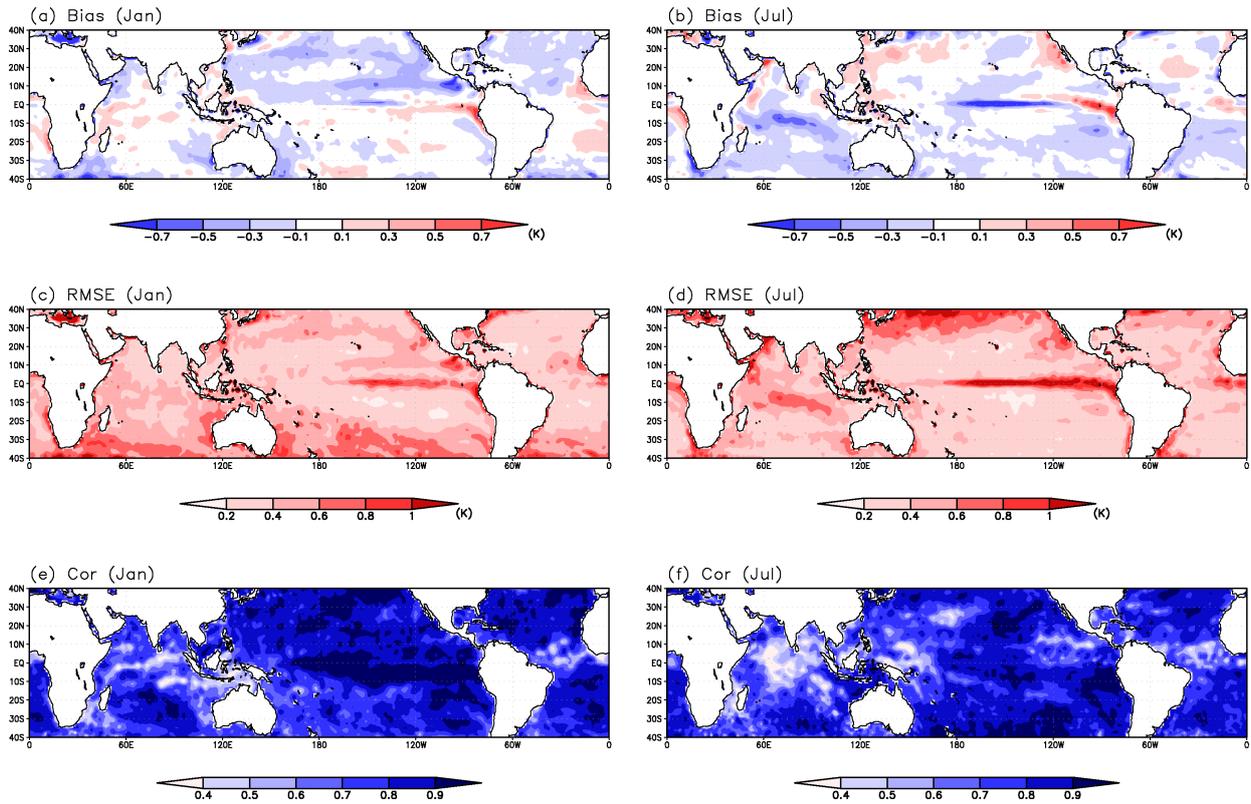
Figure 8: Deterministic scores of SST on day 10 for (a, c, e) January cases and (b, d, f) July cases: (a, b) mean bias, (c, d) root mean square error, (e, f) correlation.
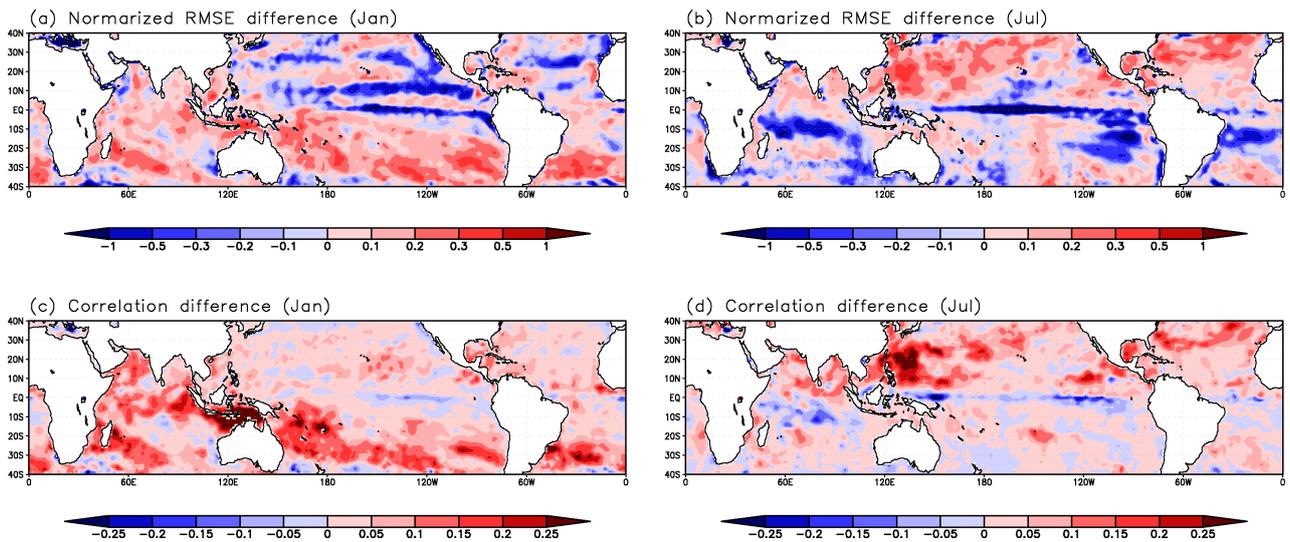

Figure 9: Difference of deterministic scores of SST on day 10 for (a, c) January cases and (b, d) July cases: (a, b) normalised RMSE difference, (c, d) anomaly correlation difference (KPP-CNT).

forecasts starting from the 1st of February, May, August and November 1989–2007 have been produced. The control experiment (CTRL) has the same configurations as the operational system. In a test experiment (KPP), the ocean mixed layer model is used in the first 10 days of integrations. After day 10, IFS is coupled to the ocean model HOPE as in the control experiment and the operational system.

Tables 1–4 display the Brier scores and relative operating characteristic (ROC) scores of 2-m temperature, precipitation, 850-hPa temperature and 500-hPa geopotential height for day 5-11, day 12-18, day 19-25 and day 26-32. Overall the impact of the ocean mixed layer model on the forecast skill is neutral. For temperature and winds, the impact is not statistically significant. Although they are not statistically significant, the day 5-11 scores of precipitation, 850-hPa temperature of the KPP experiment are consistently improved in most regions. As far as we know, this is the first result showing potential improvements of the medium-range atmospheric forecasts when coupling atmospheric models to an ocean model (mixed-layer model or OGCM). On the other hand, the ROC and Brier scores show degradations in day 26-32 500-hPa geopotential height forecasts when using the KPP model. These degradations may be due to the less skillful SST forecasts in the equatorial Pacific (Figure 9). A larger set of hindcasts would be needed to assess the impact of ocean-atmosphere coupling on medium-range forecasts with more details.

The skin layer scheme (Zeng and Beljaars, 2005) was applied to the control forecast in our comparison. This may explain why the ocean coupling has such a small impact in the first 10-days, since the skin layer scheme simulates the SST diurnal cycle in the control experiment. Although the improvements in global forecasts scores are rather small, an impact can be seen in some atmospheric severe events. Recently Lebeaupin et al. (2009) have tested a Metéo France MESO-NH model coupled with a one-dimensional ocean mixed layer model using a TKE scheme (Gaspar et al. 1990). They found that the ocean coupling tends to weaken the severe convective activity and the rainfall intensity in their short range forecasts, although the impact is moderate. Since the KPP model is not currently fully coupled in the midlatitudes because of large SST errors, we have not investigated the heavy rain events as in Lebeaupin et al. (2009) yet. The air-sea interaction in extratropical cyclones, mesoscale disturbances and heavy rain events will be investigated in future research.

3.4   MJO experiment

The skill to predict the evolution of the MJO has been assessed with the cycle 35r2 with and without the KPP model. Although many studies have already pointed out that atmosphere-ocean coupled models have a better representation of the MJO propagation and organisation, it is worth confirming these results with the same configuration as the operational system. Five-member ensemble forecasts starting at 00Z from 15 December 1992 to 31 January 1993 have been performed. The control experiment uses the same configuration as the operational EPS with the cycle 35r2. The model settings are the same as in section 3.3. It should be noted that the cycle 35r2 uses the skin layer scheme (Zeng and Beljaar, 2005). Therefore this version of IFS simulates the diurnal cycle of SST. The model resolutions is T399L62 during the first 10 days and T255L62 after day 10. In the test experiment (KPP), the KPP model is coupled to IFS during the first 10-day forecasts instead of using persisted SST anomalies. After day 10, IFS is coupled to the HOPE ocean model as in the control experiment. The MJO forecast skill is assessed using MJO indices as in Wheeler and Hendon (2004). The MJO indices are calculated by projecting the forecasts onto combined EOFs of 200-hPa, 850-hPa zonal wind and outgoing longwave radiation calculated using NCEP re-analysis. Figure 14 shows the first and second combined EOFs. The linear correlation between the predicted and observed PC1 and PC2 (Figure 14) as a function of the forecast lead time are consistently improved beyond day-9 (Figure 15) when coupling IFS to the KPP model. This result agrees with Vitart et al. (2007) and Woolnough et al. (2007), although the difference between the control and test experiment is smaller than in their results. This difference may have several explanations. Firstly, the KPP model is used in only the first 10 days, instead of the first 32 days as in Vitart et al. (2007). Secondly, the MJO
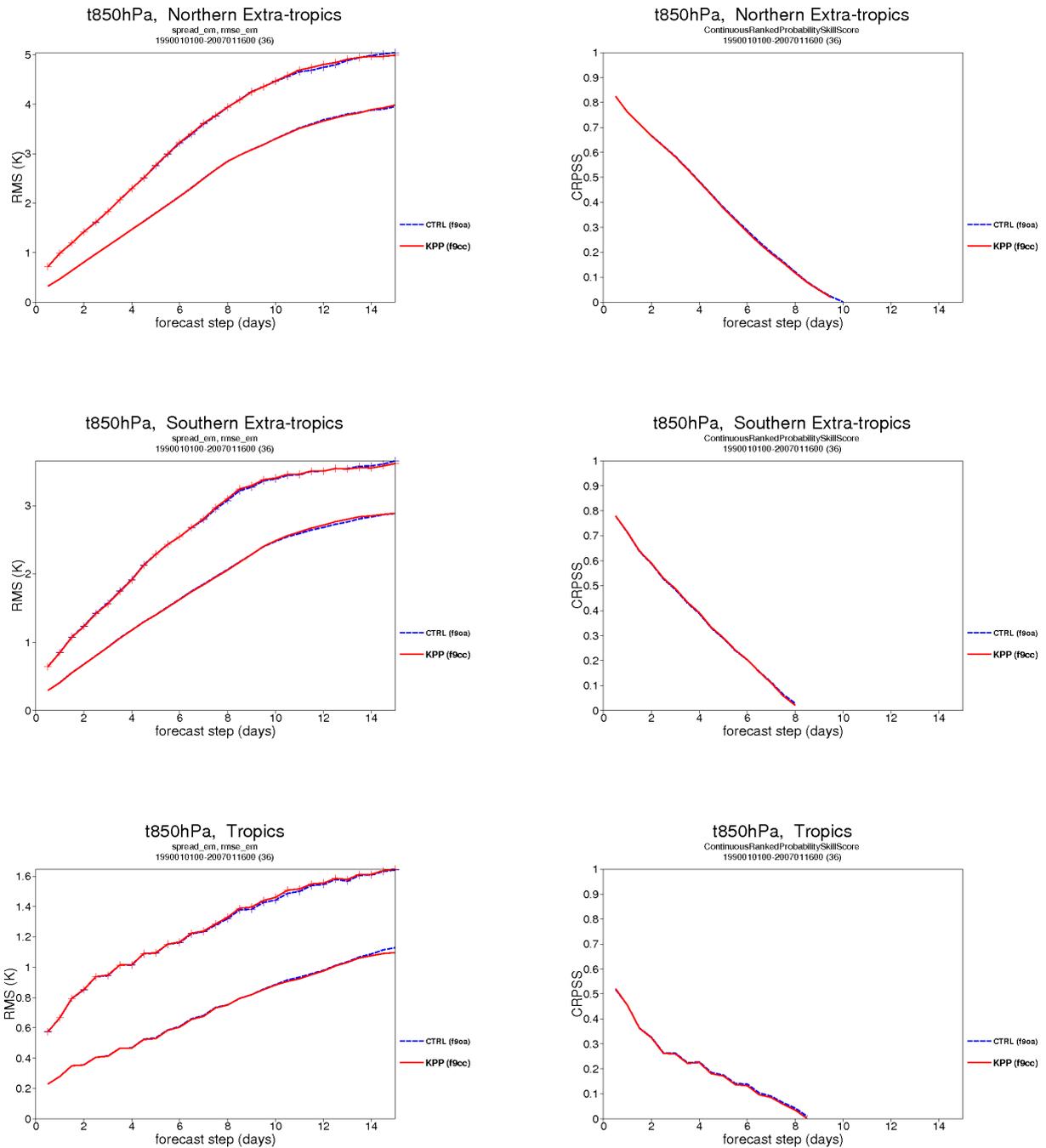
Figure 10: RMSE, continuous ranked probability skill score (CRPSS) for temperature at 850 hPa in January: (upper) northern extratropics (20°N–90°N), (middle) southern extratropics (20°S-90°S), (bottom) tropics (20°N–20°S). Blue and red lines show the control experiment and KPP experiment, respectively.

Figure 11: RMSE, CRPSS for geopotential height at 500 hPa in January.

Figure 12: Same as Figure 10, but for July.

Figure 13: Same as Figure 13, but for July.

Brier scores for 2m temperature, upper tercile

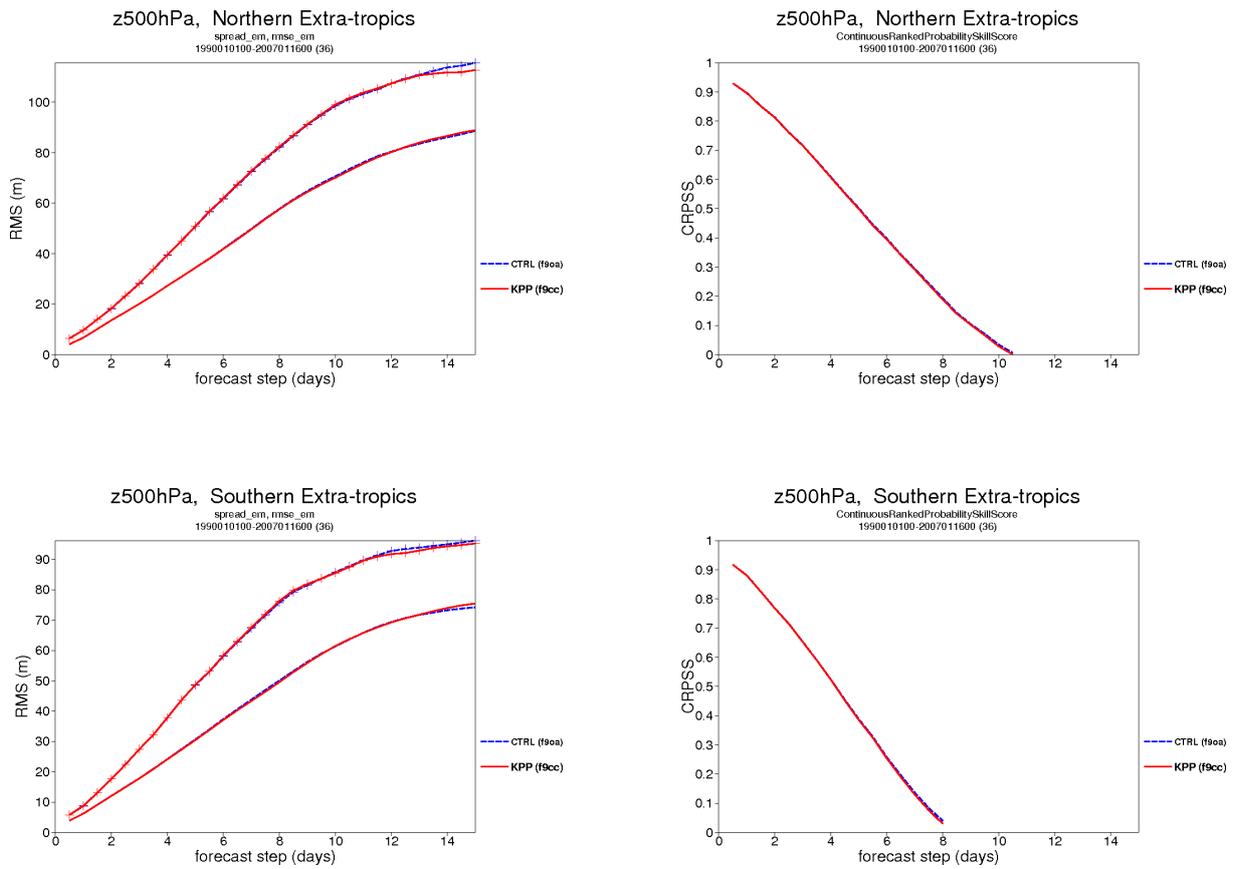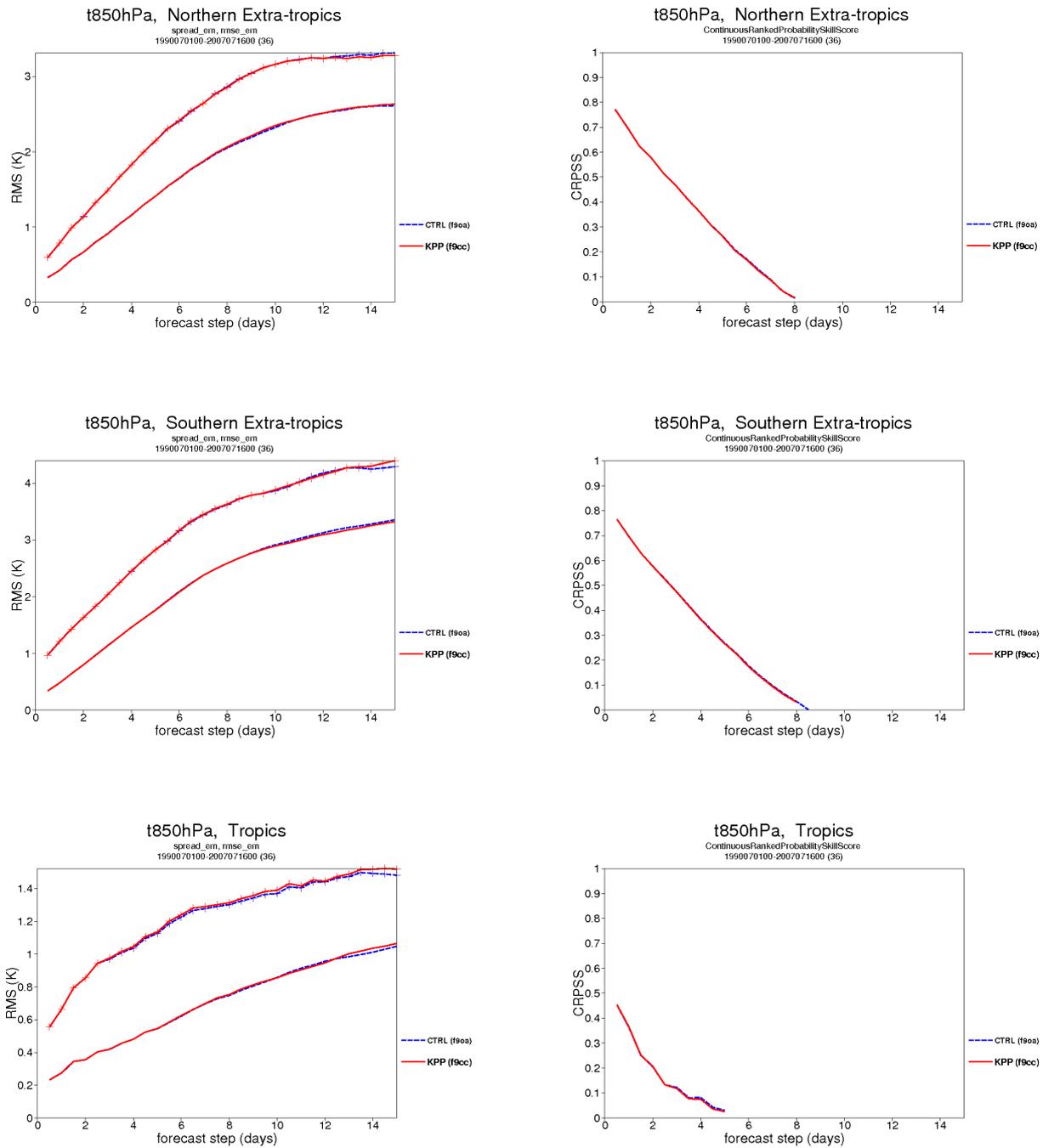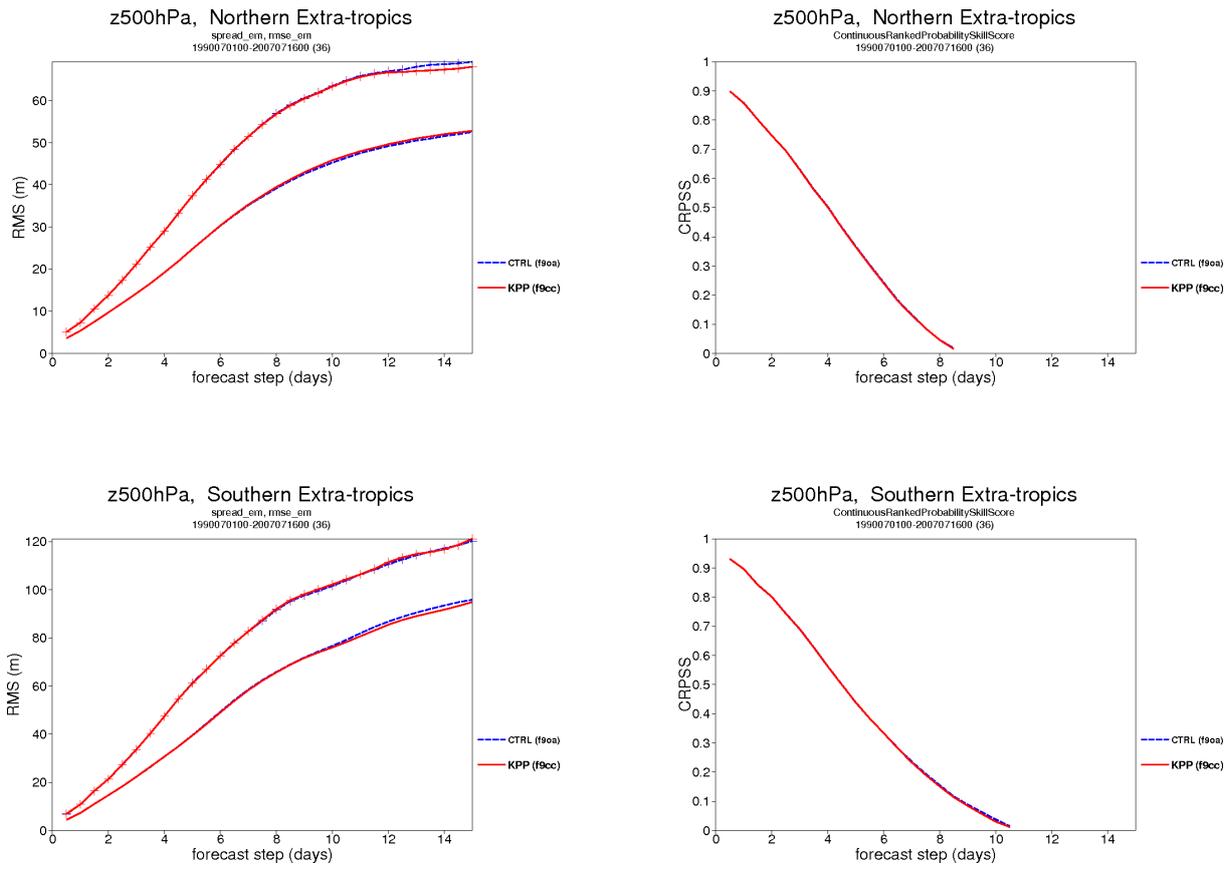| Regions	week 1 KPP	week 1 CTRL	week 2 KPP	week 2 CTRL	week 3 KPP	week 3 CTRL	week 4 KPP	week 4 CTRL
Northern Extratropics	0.137	0.137	**0.212**	0.214	**0.233**	0.235	0.239	**0.235**
Southern Extratropics	**0.166**	0.167	0.230	**0.221**	**0.240**	0.246	**0.239**	0.243
Tropics	0.154	**0.153**	0.197	0.197	0.218	0.218	0.226	**0.225**
Europe	0.127	**0.126**	**0.211**	0.216	0.238	**0.237**	**0.237**	0.229
North America	**0.132**	0.133	**0.217**	0.218	**0.229**	0.233	**0.228**	0.231

Brier scores for 2m temperature, lower tercile

Regions	week 1 KPP	week 1 CTRL	week 2 KPP	week 2 CTRL	week 3 KPP	week 3 CTRL	week 4 KPP	week 4 CTRL
Northern Extratropics	**0.140**	0.141	**0.209**	0.211	**0.232**	0.235	0.240	**0.239**
Southern Extratropics	0.167	**0.165**	0.230	**0.224**	**0.240**	0.243	0.245	**0.243**
Tropics	0.153	0.153	**0.199**	0.201	0.222	**0.221**	0.228	0.228
Europe	**0.125**	0.126	**0.217**	0.220	0.244	**0.241**	**0.239**	0.242
North America	0.147	0.147	0.215	**0.211**	**0.225**	0.230	**0.234**	0.238

Brier scores for precipitation, upper tercile

Regions	week 1 KPP	week 1 CTRL	week 2 KPP	week 2 CTRL	week 3 KPP	week 3 CTRL	week 4 KPP	week 4 CTRL
Northern Extratropics	0.212	0.212	**0.238**	0.239	0.244	**0.242**	0.245	0.245
Southern Extratropics	**0.225**	0.226	0.245	**0.240**	**0.240**	0.244	0.239	**0.238**
Tropics	0.249	0.249	**0.265**	0.267	**0.276**	0.278	**0.277**	0.280
Europe	**0.201**	0.202	**0.241**	0.242	0.243	**0.242**	0.247	**0.246**
North America	0.216	0.216	0.240	**0.236**	0.241	**0.238**	0.242	0.242

Brier scores for precipitation, lower tercile

Regions	week 1 KPP	week 1 CTRL	week 2 KPP	week 2 CTRL	week 3 KPP	week 3 CTRL	week 4 KPP	week 4 CTRL
Northern Extratropics	0.212	0.212	**0.238**	0.241	0.242	**0.241**	0.246	**0.244**
Southern Extratropics	0.231	0.231	0.242	**0.240**	**0.238**	0.241	**0.239**	0.241
Tropics	0.248	0.248	**0.262**	0.263	**0.270**	0.271	0.267	0.267
Europe	0.196	0.196	**0.240**	0.241	**0.242**	0.244	0.244	**0.243**
North America	0.213	0.213	**0.239**	0.241	0.240	0.240	0.243	**0.241**

Table 1: Brier scores of 2-m temperature and precipitation for 15-member EPS forecasts starting the 1st of February, May, August and November 1989-2008. The KPP experiment (KPP) and the control experiment (CTRL) are shown. The figures in bold show better scores with KPP than with CTRL.

Brier scores for 850-hPa temperature, upper tercile

Regions	week 1		week 2		week 3		week 4	
	KPP	CTRL	KPP	CTRL	KPP	CTRL	KPP	CTRL
Northern Extratropics	0.134	0.134	0.214	0.214	**0.233**	0.236	0.239	**0.236**
Southern Extratropics	0.161	0.161	0.232	**0.224**	**0.246**	0.249	**0.243**	0.247
Tropics	0.142	0.142	0.194	**0.193**	0.214	0.214	**0.223**	0.224
Europe	**0.132**	0.134	**0.220**	0.222	0.241	**0.235**	0.241	**0.233**
North America	0.132	**0.131**	0.214	**0.213**	**0.228**	0.238	**0.229**	0.232

Brier scores for 850-hPa temperature, lower tercile

Regions	week 1		week 2		week 3		week 4	
	KPP	CTRL	KPP	CTRL	KPP	CTRL	KPP	CTRL
Northern Extratropics	**0.134**	0.135	**0.209**	0.212	**0.234**	0.237	0.241	**0.239**
Southern Extratropics	**0.161**	0.162	0.230	**0.225**	0.244	0.244	0.245	**0.243**
Tropics	**0.140**	0.141	**0.194**	0.195	0.218	**0.217**	**0.226**	0.227
Europe	**0.124**	0.126	**0.218**	0.222	0.247	**0.244**	**0.241**	0.242
North America	0.136	0.136	0.208	0.208	**0.222**	0.231	**0.230**	0.237

Brier scores for 500-hPa geopotential height, upper tercile

Regions	week 1		week 2		week 3		week 4	
	KPP	CTRL	KPP	CTRL	KPP	CTRL	KPP	CTRL
Northern Extratropics	0.128	0.128	0.211	0.211	**0.235**	0.236	0.242	**0.239**
Southern Extratropics	**0.143**	0.145	0.207	**0.206**	**0.235**	0.243	0.254	**0.242**
Europe	**0.121**	0.123	**0.228**	0.229	0.241	**0.236**	0.239	**0.237**
North America	0.135	0.135	**0.212**	0.215	**0.234**	0.237	0.231	**0.230**

Brier scores for 500-hPa geopotential height, lower tercile

Regions	week 1		week 2		week 3		week 4	
	KPP	CTRL	KPP	CTRL	KPP	CTRL	KPP	CTRL
Northern Extratropics	0.132	0.132	0.210	0.210	**0.233**	0.236	0.242	**0.239**
Southern Extratropics	0.157	0.157	**0.215**	0.217	**0.233**	0.245	0.244	0.244
Europe	0.127	0.127	**0.221**	0.225	0.243	**0.239**	0.242	**0.234**
North America	0.140	0.140	0.207	**0.205**	**0.224**	0.233	0.234	**0.230**

Table 2: Same as Table 1 but for 850-hPa temperature and 500-hPa geopotential height.

ROC scores for 2-m temperature, upper tercile

Regions	week 1		week 2		week 3		week 4	
	KPP	CTRL	KPP	CTRL	KPP	CTRL	KPP	CTRL
Northern Extratropics	0.870	0.870	**0.685**	0.679	**0.591**	0.585	0.551	**0.567**
Southern Extratropics	**0.816**	0.814	0.616	**0.640**	**0.546**	0.523	**0.536**	0.519
Tropics	0.847	**0.848**	0.739	**0.740**	0.667	**0.669**	0.631	**0.634**
Europe	0.888	**0.889**	**0.681**	0.668	0.566	0.566	0.551	**0.582**
North America	0.877	0.877	**0.669**	0.665	**0.602**	0.591	**0.598**	0.587

ROC scores for 2-m temperature, lower tercile

Regions	week 1		week 2		week 3		week 4	
	KPP	CTRL	KPP	CTRL	KPP	CTRL	KPP	CTRL
Northern Extratropics	0.864	0.864	**0.690**	0.686	**0.591**	0.580	0.549	**0.551**
Southern Extratropics	0.816	**0.819**	0.619	**0.633**	**0.543**	0.532	0.513	**0.522**
Tropics	0.846	0.846	**0.732**	0.728	0.651	**0.657**	0.622	**0.625**
Europe	**0.889**	0.888	**0.670**	0.664	0.537	**0.547**	**0.543**	0.528
North America	0.855	0.855	0.673	**0.682**	**0.616**	0.600	**0.575**	0.561

ROC scores for precipitation, upper tercile

Regions	week 1		week 2		week 3		week 4	
	KPP	CTRL	KPP	CTRL	KPP	CTRL	KPP	CTRL
Northern Extratropics	**0.703**	0.702	**0.574**	0.570	0.531	**0.538**	0.514	0.514
Southern Extratropics	**0.670**	0.669	0.537	**0.554**	**0.524**	0.511	0.528	**0.531**
Tropics	**0.695**	0.694	**0.617**	0.615	**0.571**	0.570	**0.546**	0.541
Europe	**0.729**	0.728	**0.564**	0.557	0.526	0.526	0.502	**0.504**
North America	**0.685**	0.684	0.554	**0.566**	0.531	**0.538**	0.517	**0.519**

ROC scores for precipitation, lower tercile

Regions	week 1		week 2		week 3		week 4	
	KPP	CTRL	KPP	CTRL	KPP	CTRL	KPP	CTRL
Northern Extratropics	**0.704**	0.703	**0.572**	0.561	0.534	**0.539**	0.510	**0.516**
Southern Extratropics	**0.663**	0.662	0.543	**0.548**	**0.539**	0.524	**0.524**	0.516
Tropics	0.689	0.689	**0.610**	0.607	0.558	**0.560**	0.544	0.544
Europe	**0.746**	0.745	**0.565**	0.560	**0.530**	0.521	0.515	0.515
North America	0.693	0.693	**0.556**	0.549	**0.533**	0.532	0.516	**0.524**

Table 3: ROC scores of 2-m temperature and precipitation for 15-member EPS ensemble forecasts starting the 1st of February, May, August and November 1989–2008 for the KPP (KPP) and the control experiment (CTRL). The figures in bold font shows better scores for KPP than CTRL.

ROC scores for 850-hPa temperature, upper tercile

	week 1		week 2		week 3		week 4	
Regions	KPP	CTRL	KPP	CTRL	KPP	CTRL	KPP	CTRL
Northern Extratropics	**0.876**	0.875	**0.672**	0.670	**0.576**	0.569	0.540	**0.554**
Southern Extratropics	0.825	0.825	0.603	**0.625**	**0.517**	0.510	**0.518**	0.508
Tropics	**0.866**	0.865	0.746	**0.749**	0.672	**0.674**	0.630	0.630
Europe	**0.877**	0.875	**0.648**	0.645	0.543	**0.564**	0.528	**0.561**
North America	0.879	**0.880**	0.670	**0.673**	**0.590**	0.560	**0.584**	0.572

ROC scores for 850-hPa temperature, lower tercile

	week 1		week 2		week 3		week 4	
Regions	KPP	CTRL	KPP	CTRL	KPP	CTRL	KPP	CTRL
Northern Extratropics	**0.874**	0.873	**0.683**	0.675	**0.574**	0.562	0.536	**0.541**
Southern Extratropics	**0.826**	0.824	0.617	**0.624**	**0.529**	0.524	0.510	**0.513**
Tropics	**0.866**	0.865	**0.742**	0.741	0.660	**0.663**	**0.625**	0.622
Europe	**0.890**	0.888	**0.660**	0.647	0.515	**0.524**	**0.529**	0.520
North America	**0.873**	0.872	0.683	**0.685**	**0.619**	0.583	**0.580**	0.554

ROC scores for 500-hPa geopotential height, upper tercile

	week 1		week 2		week 3		week 4	
Regions	KPP	CTRL	KPP	CTRL	KPP	CTRL	KPP	CTRL
Northern Extratropics	0.885	0.885	0.678	0.678	**0.572**	0.570	0.533	**0.542**
Southern Extratropics	**0.853**	0.849	0.694	**0.700**	**0.578**	0.555	0.487	**0.535**
Europe	**0.897**	0.895	**0.624**	0.621	0.540	**0.563**	0.535	**0.547**
North America	0.872	0.872	**0.678**	0.670	**0.573**	0.558	0.575	**0.584**

ROC scores for 500-hPa geopotential height, lower tercile

	week 1		week 2		week 3		week 4	
Regions	KPP	CTRL	KPP	CTRL	KPP	CTRL	KPP	CTRL
Northern Extratropics	0.877	0.877	0.683	**0.684**	**0.578**	0.569	0.529	**0.544**
Southern Extratropics	0.845	0.845	**0.673**	0.665	**0.593**	0.556	**0.533**	0.514
Europe	0.887	0.887	**0.651**	0.636	0.524	**0.543**	0.529	**0.554**
North America	0.864	0.864	0.686	**0.695**	**0.612**	0.582	0.562	**0.584**

Table 4: Same as Table 3 but for 850-hPa temperature and 500-hPa geopotential height.

Combined EOF1
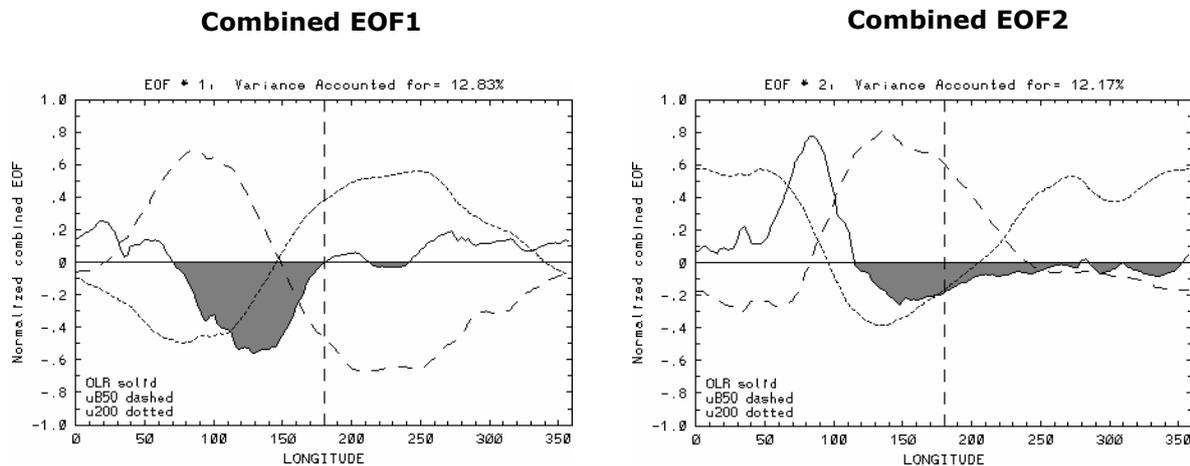
Combined EOF2

Figure 14: Combined EOF 1 (PC1) and 2 (PC2) of observed OLR and zonal wind at 850 and 200 hPa averaged between 15N and 15S (Vitart and Molteni 2009a).

forecast skill depends on the IFS version (Vitart and Molteni 2009b), so the degree of MJO improvements with the KPP model may also depend on the IFS version. Thirdly the diurnal cycle of SST, which contributes to more skilful MJO forecasts, is simulated by the skin layer scheme in the control experiment. Even so, the test experiment suggests improved forecast skill in the KPP experiment compared with the control experiment. This implies that the SST variability at a medium-range time scale may have additional benefits for MJO forecasts than just the representation of the SST diurnal cycle as seen in section 3.1.

3.5   Impact of the KPP model on the Indian monsoon rainfall in early summer

In the boreal summer, the air-sea interaction plays an important role in the monsoon variability over the Indian Ocean. Indian monsoon rainfall is difficult to predict well with NWP models. Recently, Vitart and Molteni (2009a) have reported that the ocean mixed layer model coupled to IFS improves the forecast skill of the Indian monsoon rainfall in the early summer.

A series of 46-day ensemble forecasts has been performed with the IFS cycle 35r2 to confirm Vitart and Molteni (2009a), which used the cycle 32r2. The skin layer scheme (ZB05) was not used in the cycle 32r2. In the cycle
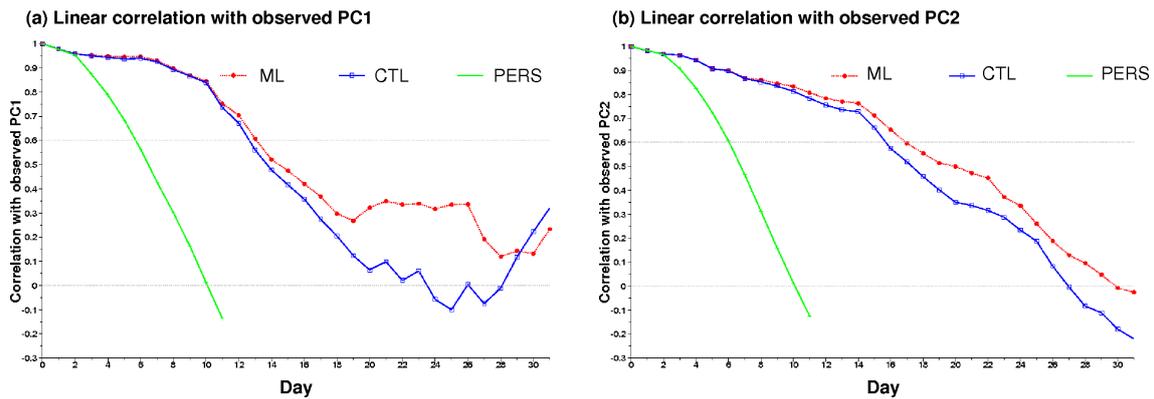
Figure 15: Linear correlation with the observed MJO (a) PC1 and (b) PC2 patterns.

35r2, the skin layer scheme is activated unless the KPP model is used. In the control experiments VEPS1 (cycle 32r2) and VEPS2 (cycle 35r2), the configuration is the same as in the operational system (persisted SST anomalies during the first 10 days and the fully coupled after day 10) (Vitart et al., 2008). In the KPP experiment with the cycle 32r2 (ML1), the IFS is coupled to the KPP model for 32 days. On the other hand, the KPP experiment with the cycle 35r2 (ML2) is coupled to the KPP model during the first 10 days and is coupled to the OGCM after 10 days. The experimental settings are listed in Table 5. Each experiment consists of 15-member ensemble integrations starting from 15 May 1991–2007.

Table 6 shows the forecast scores of precipitation over India (70–85 °E, 5–30 °N, blue box in Figure 16) in June during 1991–2007. The correlation with the India Meteorological Department (IMD) station rainfall data over India is improved when using the cycle 35r2 instead of the cycle 32r2 and it is also improved when coupling IFS to the KPP model. However, the difference between the control and test experiments is smaller with the cycle 35r2 than with the cycle 32r2. The test experiment with the cycle 35r2 (ML2) has the best correlation score. On the other hand, the KPP model does not improve the RMSE with the cycle 35r2. Better air-sea interaction in coupled models (Fu et al. 2003) may contribute to the improvement of forecast scores of precipitation over India.

3.6   Impact of ocean coupling on tropical cyclone forecasts

Extreme phenomena such as tropical cyclones can strongly interact with the upper-ocean even at the short-range time scale. Observational studies have shown that tropical cyclones can generate a cooling up to several degrees at the surface of the ocean (Leipper 1967; Stramma et al. 1986; Wentz et al. 2000). Numerical simulation studies have revealed that the cooling is caused by the entrainment mixing and surface cooling (e.g., Chang and Anthes 1978; Price 1981; Wada 2005). Furthermore it has been demonstrated that the ocean cooling

| Experiments | IFS cycle | 0–10 days | | 10–32 days | |
		resolution	ocean coupling	resolution	ocean coupling
VEPS1	32r2	T399	none	T255	HOPE
ML1	32r2	T159	KPP	T159	KPP
VEPS2	35r2	T399	ZB05	T255	HOPE
ML2	35r2	T399	KPP	T255	HOPE

Table 5: Experimental set-ups in the early Indian monsoon rainfall experiments.
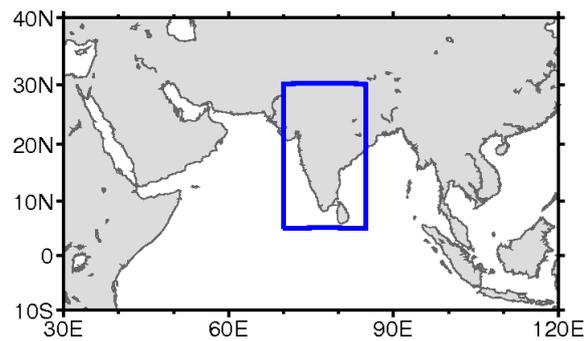
Figure 16: All Indian Rainfall area (70–85 °E, 5–30 °N).

	VEPS1	ML1	VEPS2	ML2
Correlation	0.57	0.62	0.63	0.67
RMSE (mm/day)	0.92	0.84	0.98	1.05

Table 6: Forecast scores for Indian monsoon rainfall in June 1990–2007. The ensemble mean of 15-member integrations starting from 15 May is verified against IMD station data. The scores with the cycle 32r2 (VEPS1, ML1) are presented in Vitart and Molteni (2009a).

can weaken the intensity of tropical cyclones (e.g., Bender et al. 1993; Wada 2009).

A case study with a high resolution T1279 deterministic forecast and 51-member T639 ensemble forecasts is presented in this section. Coupled (ML) and uncoupled (CTL) 10-day integrations are carried out in order to investigate effects of ocean coupling on tropical cyclone forecasts. The forecasts start on 14, 15 and 16 September 2009 for super typhoon Choi-Wan. In this case study, an ocean cooling exceeding 4 K after five days (Figure 17) is simulated in the vicinity of super typhoon Choi-Wan in the T639 ensemble and T1279 deterministic forecasts coupled to the KPP model. However, the ocean cooling is smaller in the forecasts than in the TMI satellite observation. The intensity based on minimum sea level pressure and maximum wind speed is consistently weakened by coupling the KPP model (Figure 18) in agreement with previous studies(e.g., Bender et al. 1993; Wada 2009). The impact of the KPP coupling on the forecast of another strong typhoon, typhoon Melor 2009 has also been investigated. The ocean cooling is weaker for typhoon Melor than for typhoon Choi-Wan and the impact of the KPP model on the intensity of the typhoon is not significant for this case. We think that the faster translation speed and less ocean cooling as a result may be associated with less impact on the intensity. There is minor impact on tropical cyclone tracks in both cases, which agrees with Wu et al. (2005).

The impact of ocean coupling on the intensity of tropical cyclones has also been evaluated using ensemble forecasts with a T399 resolution for 45 tropical cyclone cases in 2008. Figures 19a and 19b are scatter plot-diagrams of minimum sea level pressure and maximum 10-m wind speed, respectively. In Figure 19a, the ocean mixed layer coupled model predicts lower sea level pressure than the uncoupled model for strong tropical cyclones (75 % chances for < 980 hPa). In Figure 19b, the coupled model predicts lower 10-m wind speed than the uncoupled model (85 % chance for > 40 m s^{-1}). Therefore, the ocean coupling weakens the intensity of strong tropical cyclones in the numerical model.

Although the ocean cooling by tropical cyclones is simulated by the KPP model as in Price et al. (1981) and Emanuel (1999), the amplitude of the ocean cooling is smaller in the model than in the TMI observation for typhoon Choi-wan. In fact, it has been pointed out that a one-dimensional model underestimates the ocean cooling due to the lack of upwelling (Yablonsky and Ginis 2009). The implemented ocean mixed layer model does not represent the upwelling, which may be a reason for the underestimation of the ocean cooling in this
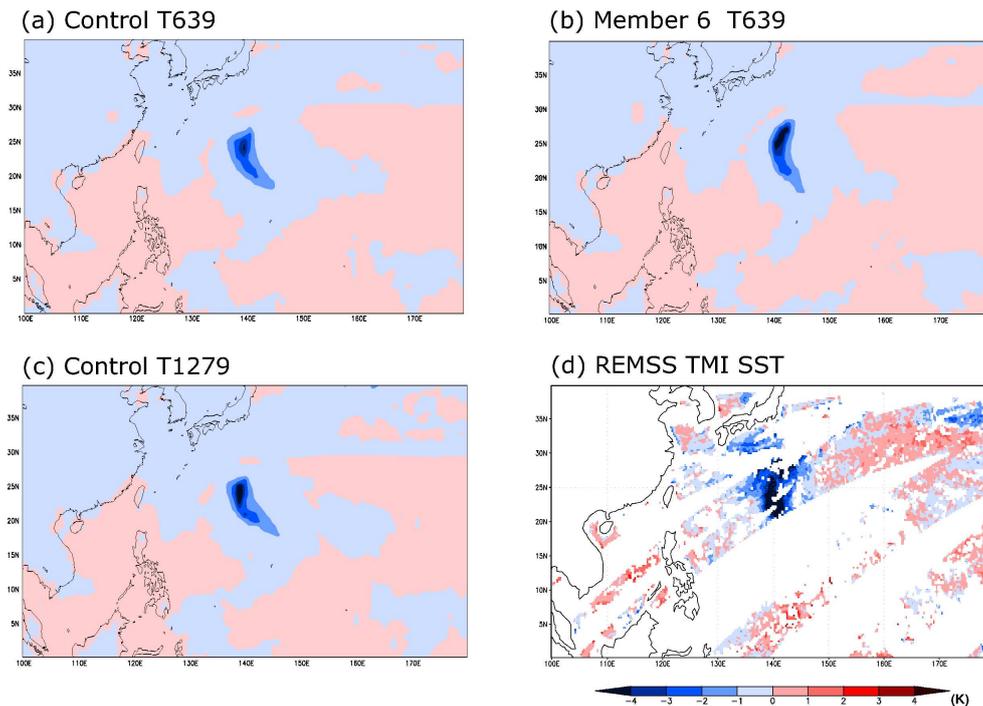
Figure 17: SST change from 14/09/2009 to 18/09/2009 in (a)T639 control forecast, (b)T639 ensemble member with the largest SST cooling in ensemble members, (c)T1279 control forecast, (d)REMSS TMI data.

model.

The horizontal resolution of the current operational EPS (T639) is insufficient to simulate realistic intensity of strong tropical cyclones (not shown). Hence it is found that coupling IFS to the ocean model is likely to degrade the forecast of the intensity of strong tropical cyclones at the current resolution of the operational EPS. Since the air-sea interaction has an impact on the intensity of tropical storms in real situations, this process should be included in future high-resolution forecast systems.

3.7   Assessment of the diurnal cycle of SST

Accuracy of SST is crucial for numerical weather prediction and assimilation. Fairall et al. (1996) noted that SST with an accuracy of 0.2 degrees is required to evaluate the heat exchange of the upper ocean with an accuracy of 10 W m^{-2}. The atmosphere interacts with the ocean via so-called skin SST (Donlon et al. 2007), which is defined as temperature at the water surface. Skin SST has a large diurnal variability, therefore the skin SST should be simulated in numerical weather prediction and assimilation to give more accurate estimate of surface fluxes.

The diurnal cycle of SST is expected to have a significant influence on the atmospheric variability from diurnal to intraseasonal time scales (e.g., Kawai and Wada 2007). The diurnal cycle of SST also modulates mean climate of atmospheric models (Brunke et al. 2008). Thus, the representation of diurnal cycle of SST should contribute to a more realistic simulation of the climate mean state and variability.

There have been several attempts to simulate the diurnal variability of SST with numerical models, ranging from relatively simple skin layer schemes (e.g., Fairall et al. 1996; Webster et al. 1996; Zeng and Beljaars 2005), one-dimensional mixed layer models (e.g., Bernie et al. 2005; Kawai and Kawamura 2000; Kondo et al.
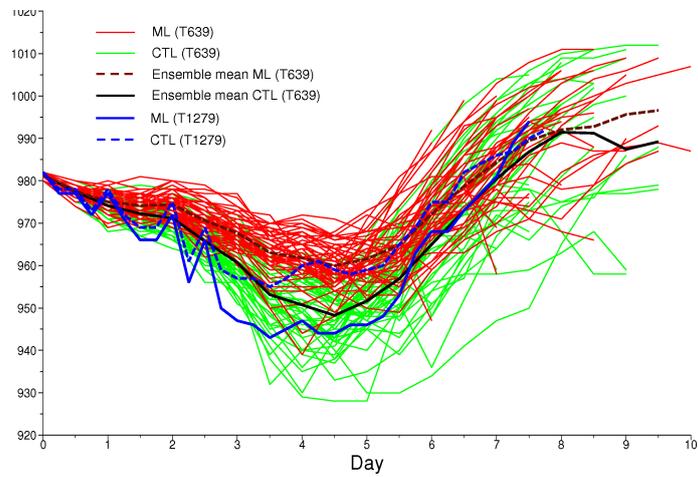
Figure 18: *Minimum mean sea level pressure of typhoon Choi-Wan in 2009. Forecasts are started from 14 September 2009.*
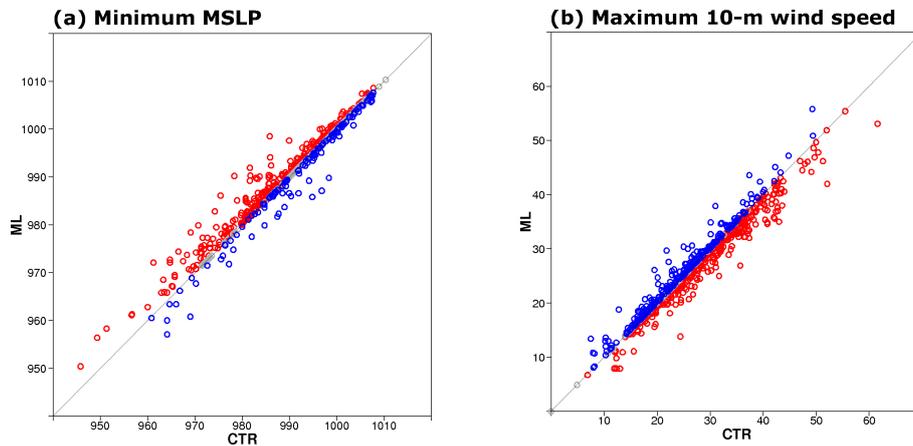

Figure 19: *Scatter plots of (a) minimum mean sea level pressure and (b) maximum 10-m wind speed during 10-day tropical cyclone forecasts for 45 cases in 2008. The x-axis represents the intensity of the tropical cyclones in the control experiment and the y-axis represents the intensity of the tropical cyclones in the KPP experiment. Red (blue) circles indicate that the intensity of tropical cyclones are weaker (stronger) in the coupled model than the uncoupled model.*
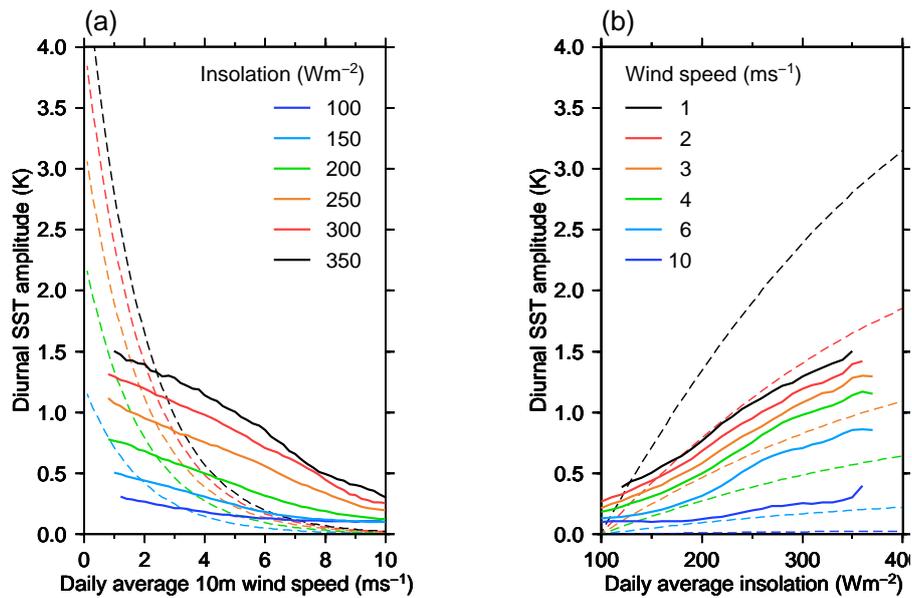
Figure 20: The averaged DSA of the KPP model. The DSA is stratified with daily average surface insolation and 10 m wind speed. (a) The DSA for given daily average insolation with respect to 10 m wind speed. (b) The DSA for given daily average 10 m wind speed with respect to insolation. Solid (dashed) lines show the model results (satellite estimates from Gentemann et al. (2003)). Bin intervals are 10 W m^{-2} for insolation and 0.2 m s^{-1} for 10 m wind speed. Data is only plotted when the sample size is more than 100.

1979; Pimentel et al. 2008) or OGCMs (Bernie et al. 2007; Danabasoglu et al. 2006). But an intercomparison of these models has not been carried out yet.

In this section, we diagnose the diurnal variability of SST in the KPP model for future applications such as weather/monthly forecasts and coupled data assimilation. Sets of SST simulations at a T255 resolution, with initial conditions on 1 January and July 1990–2007, are analysed by means of the method described in Takaya et al. (2010). The hourly outputs in 30 °N–30 °S are used for the diagnostics. In this analysis, the diurnal SST amplitude (DSA) is defined as in section 3.1. The reference data is the satellite estimate from the TMI satellite observation (Gentemann et al. 2003). The satellite estimate is obtained together with the shortwave radiation at the top of atmosphere, therefore the value of the shortwave flux at the top of atmosphere (Q in equation 1a of Gentemann et al. (2003) is simply replaced by the surface shortwave flux divided by 0.75 (for further discussion, please see section 3 of Bellenger and Duvel (2009)).

The DSA is about 1.5 K for low wind and clear sky conditions (Figure 20). Comparison with the TMI satellite estimate indicates that the model underestimates the amplitude in low wind conditions, and overestimates the amplitude in moderate and high wind conditions. The underestimation of DSA may result from the fact that the model can not represent the steep temperature gradient near the surface (Gentemann et al. 2009). On the contrary, the DSA is overestimated under high wind conditions because the mixing in high wind conditions is too weak in this model. Bernie et al. (2005) diagnosed the DSA in the Océan PArallélisé (OPA) model with a 1-m vertical resolution, which is similar to the resolution of the KPP model used in this study. Their results exhibited a DSA of about 1.5 K in low wind conditions. Although it should be noted that their experimental settings (e.g., analysed region, uncoupled forced simulation) are different from ours, the maximum DSA in very calm and clear sky conditions in our model has similar amplitudes to their results. It is also worth noting that they demonstrated that wave breaking effects can reduce the DSA and improve the DSA response in high wind conditions.
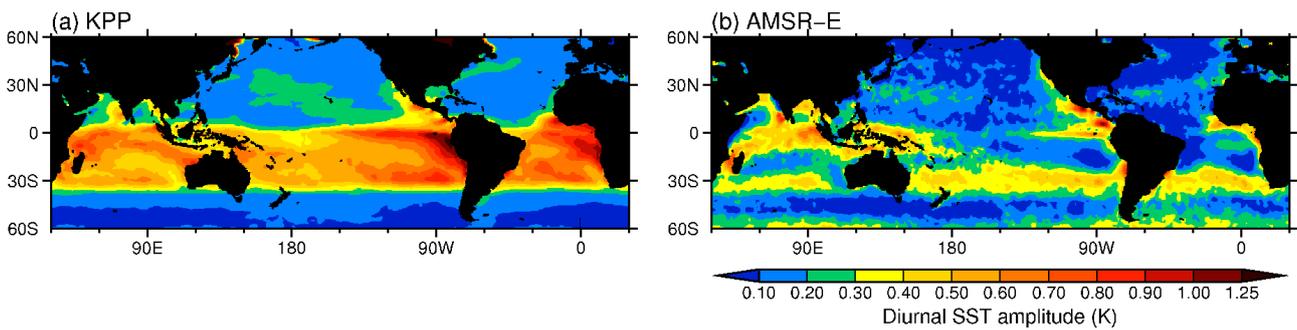
Figure 21: (Left) spatial distributions of the mean DSA for 10-day forecasts starting from the 1st of January during 1990–2007 with KPP model. (Right) spatial distribution of the day-night difference of AMSR-E ver. 5 SST averaged during 2002–2006 winter (Kawai and Wada 2007).

To evaluate the spatial distribution of the DSA resulting from the KPP model, the climatology of the DSA is compared with the AMSR-E observation (Kawai and Wada 2007). Figure 21 shows the spatial distribution of the mean DSA from the January starts of 10-day forecasts (covering the 1990–2007 period). Also shown is the spatial distribution of the day-night difference of winter AMSR-E SST (2002–2006 average), from Kawai and Wada, 2007. As seen in Figure 6, the KPP model has a broader spatial structure of the DSA. This may be because the vertical diffusion in the KPP model has too small sensitivity to wind speed (Figure 20).

The diurnal SST amplitude depends on the vertical resolution of the KPP model (Bernie et al. 2005). Additional sensitivity tests with higher resolution ($\sim$ 0.5 m for the top layer) were conducted. Results show that the higher vertical resolution improved the DSA response in calm and clear sky conditions by increasing the DSA. However, the basic characteristics of the errors (too small sensitivity to the wind speed) are similar to the results presented here. The diurnal SST response is likely to depend on the mixed layer parameterization and vertical resolution. Further development of the parameterization including wave effects together with an upgrade of vertical resolution may be needed to reproduce a better DSA response.

Meanwhile, Takaya et al. (2010) proposed modifications to the skin layer scheme of Zeng and Beljaars (2005) used to simulate the diurnal variability of skin SST. They used the same diagnostics of the DSA to demonstrate that their modified skin layer scheme reproduces the DSA quite well, at least in moderate and high wind conditions. Comparing their results with results obtained from the KPP model, the skin layer scheme seems to have an advantage in simulating the diurnal SST variability. For short-range forecasts, the skin layer scheme may be enough to account for the air-sea interaction by the diurnal SST variability. However the skin layer would not represent the air-sea interaction of the momentum flux. For forecasts at 10-day time scale, the KPP model is more suitable, although the one-dimensional approach shows its deficiencies at longer time scales. Further investigations is needed to address which approach is optimal for the daily to monthly time scales. The results presented here would suggest that the skin layer model would suffice to represent the heat-flux exchange for short-window atmospheric data assimilation.

4 Discussion

This study made an attempt to improve medium-range forecasts with coupling the ocean mixed layer model. However the verification shows minor impacts with ocean coupling. Here we discuss the impact of SST boundary conditions in a medium-range time scale. Figure 22 shows the difference of atmospheric forecast scores between a perfect SST experiment, where the SST during the forecast are the time-varying observed (analysed) SST, and a control experiment with persisted SST anomaly boundary conditions. The scores are computed

using the cycle 35r2 deterministic forecasts at a T255 resolution in 2007 (73 cases, starting from every 5 days). The NCEP OISST analysis is used, since this was the product used by operations during this period. t 850-hPa the impact of the SST forcing is only visible in the tropics, although the differences are not statistically significant. For 500-hPa geopotential height, there is no significant difference either. The impact of the SST is more visible at lower levels. At 1000-hPa, the scores are clearly better for the perfect SST experiment in northern and southern hemispheres, and tropics as well (not shown). The anomaly correlation of 1000-hPa temperature in the south hemisphere is improved up to about 0.02 after 4 days.

These results suggest a relatively small impact of SST boundary conditions on extratropic scores at short- and medium- range time scales. However it should be noted that prescribing analysed SST fields does not mean that 'perfect' SST boundary conditions given, since the air-sea interaction is not accounted for. Perfect boundary conditions are also difficult to achieve by introducing coupling with an ocean model, since errors in the SST can arise in a fully coupled model. These errors can arise from the ocean model formulation, or from deficiencies in the atmospheric fluxes. Dealing with the SST errors in the coupled model is needed to benefit from the explicit representation of the air-sea interaction in the forecasts.

5 Summary

The implementation of an ocean mixed layer model in the ECMWF IFS has been described. When coupled to the IFS, the implemented KPP ocean mixed layer model represents the diurnal cycle of SST, and predicts the SST variability at a medium-range time scale. The coupled model has positive impact in the MJO forecast as in Vitart et al. (2007) and Woolnough et al. (2007). The Indian monsoon rainfall in the early monsoon season is also improved, which is consistent with the finding by Vitart and Molteni (2009a). The impact of ocean cooling on tropical cyclones has also been examined using high resolution configurations. As many previous studies pointed out, ocean coupling tends to weaken the intensity of tropical cyclones, especially for slowly translating and intensive tropical cyclones. The coupled model is assessed in terms of the skill of EPS forecasts. The model shows improvements of SST forecast skill particularly in the summer hemisphere at a 10-day time scale. Preliminary verification of basic forecast scores indicates the overall neutral impact on forecast skill for general meteorological variables compared with an uncoupled control experiment. Although the differences are not statistically significant, scores for week 1 are consistently better in the coupled experiment than in the uncoupled control experiment. This result suggests that there may be potential for improving the medium-range forecasts by coupling with ocean models.

The representation of the diurnal SST variations have also been investigated, with implications for future applications such as data assimilation with coupled models. It was found that although the KPP model represents the diurnal cycle of SST, its performance is not as good as the simple skin layer scheme. This suggests that the simple skin layer scheme is more suitable for the short-window atmospheric data assimilation.
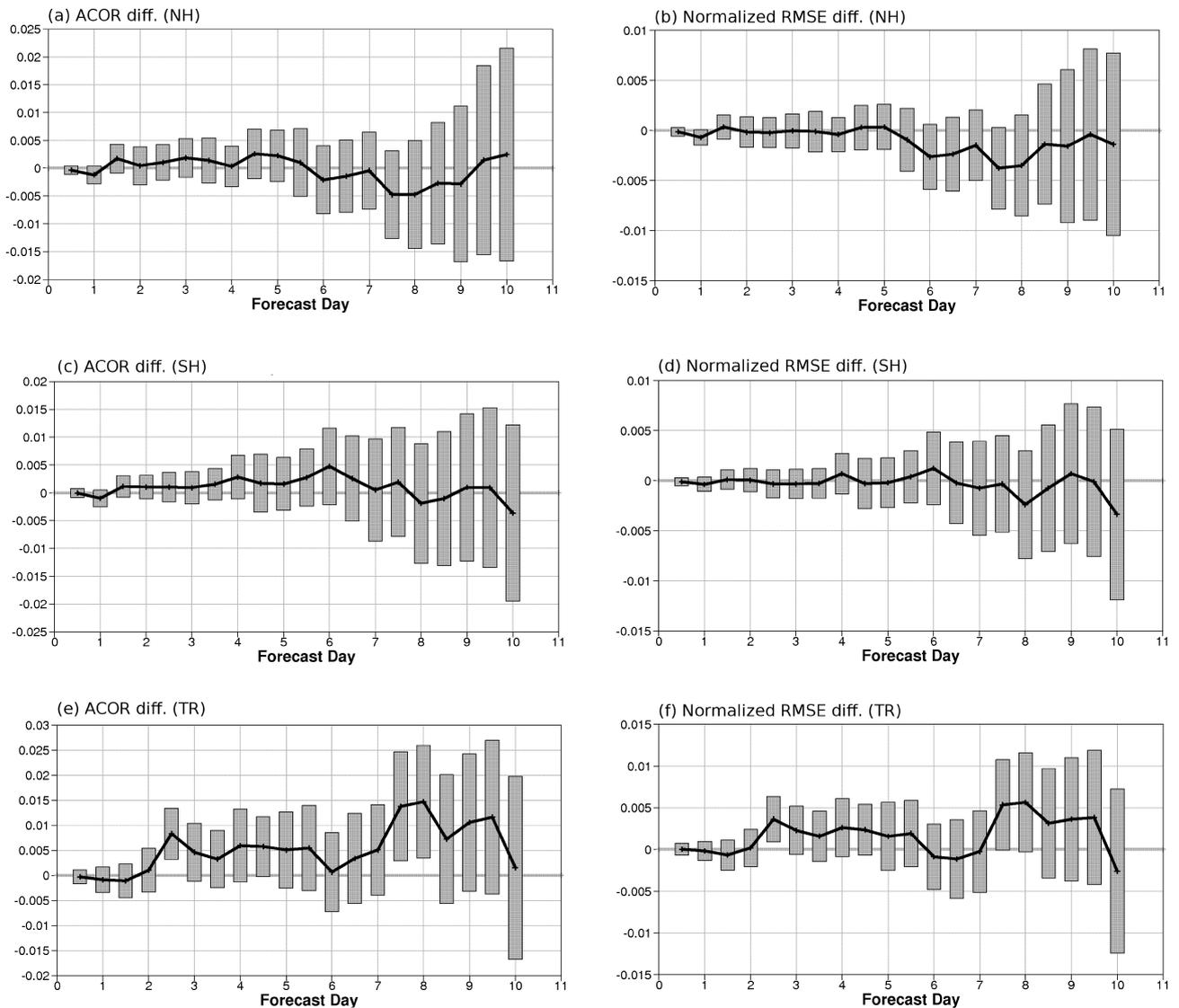
Acknowledgements

Figure 22: Difference of deterministic scores of 850-hPa temperature between the perfect SST experiment and the control forecast for (a, b) Northern hemisphere, (c, d) Southern hemisphere and (e, f) tropics: (a, c, e) anomaly correlation difference, (b, d, f) normalised RMSE difference. Positive values indicate better scores in the perfect SST experiment than the control forecast. Bars denote 95 % confidence intervals.

Reference

Balmaseda, M.A., A. Vidard, and D.L.T. Anderson (2008). The ECMWF ocean analysis system: ORA-S3. *Mon. Wea. Rev.*, 136, 3018-3034.

Bender MA, Ginis IY, Kurihara Y. (1993). Numerical simulations of tropical cyclone-ocean interaction with a high resolution coupled model. *J. Geophys. Res.*, 98:23245-63.

Bergman, J.W., H.H. Hendon, and K.M. Weickmann. (2001). Intraseasonal air-sea interactions at the onset of El Niño. *J. Climate*, 14, 1702-1719.

Bernie, D. J., S. J. Woolnough, J. M. Slingo, and E. Guilyardi (2005). Modeling diurnal and intraseasonal variability of the ocean mixed layer. *J. Climate*, 18, 1190-1202.

Bernie D. J., E. Guilyardi, G. Madec, J. M. Slingo, and S. J. Woolnough (2007). Impact of resolving the diurnal cycle in an ocean-atmosphere GCM. Part 1: A diurnally forced OGCM. *Climate Dyn.*, 29, 575-590

Brenner, S. (1996). Response of an ocean mixed layer model in 30-day December forecasts with a coupled ocean-atmosphere model. *J. Climate*, 9, 3337-3356.

Brunke, M. A., X. Zeng, V. Misra, and A. Beljaars (2008). Integration of a prognostic sea surface skin temperature scheme into weather and climate models. *J. Geophys. Res.*, 113, D21117, doi:10.1029/2008JD010607.

de Boyer Montegut, C., G. Madec, A. S. Fischer, A. Lazar, and D. Iudicone (2004). Mixed layer depth over the global ocean: An examination of profile data and a profile-based climatology. *J. Geophys. Res.*, 109, C12003, doi:10.1029/2004JC002378.

Danabasoglu, G., W.G. Large, J.J. Tribbia, P.R. Gent, B.P. Briegleb, and J.C. McWilliams (2006). Diurnal coupling in the tropical oceans of CCSM3. *J. Climate*, 19, 2347-2365.

Donald, A., H. Meinke, B. Power, A. de H. N. Maia, M. C. Wheeler, N. White, R. C. Stone, and J. Ribbe (2006). Near-global impact of the Madden-Julian Oscillation on rainfall. *Geophys. Res. Lett.*, 33, L09704, doi:10.1029/2005GL025155.

Egger J. and S. Schmid (1988). Elimination of spurious inertial oscillations in boundary-layer models with time-dependent geostrophic winds. *Boundary-Layer Meteorol.*, 43, 393–402.

Egger J. and S. Schmid (1989). Reply. *Boundary-Layer Meteorol.*, 48, 447.

Emanuel KA. (1999). Thermodynamic control of hurricane intensity. *Nature* 401:665-69.

Fairall, C. W., E. F. Bradley, D. P. Rogers, J. B. Edson, and G. S. Young (1996). Bulk parameterization of air-sea fluxes for Tropical Ocean-Global Atmosphere Coupled-Ocean Atmosphere Response Experiment. *J. Geophys. Res.*, 101(C2), 3747-3764.

Feng, M., R. Lukas, P. Hacker, R. Weller, and S. Anderson (2000). Upper-ocean heat and salt balances in the western equatorial Pacific in response to the intraseasonal oscillation during TOGA COARE. *J. Climate*, 13,

2409-2427.

Ferranti, L., T. N. Palmer, F. Molteni and E. Klinker (1990). Tropical-extratropical interaction associated with the 30-60 day oscillation and its impact on medium and extended range prediction. *J. Atmos. Sci.*, 125, 2177–2199.

Flatau, M., P.J. Flatau, P. Phoebus, and P.P. Niiler (1997). The feedback between equatorial convection and local radiative and evaporative processes: The implications for intraseasonal oscillations. *J. Atmos. Sci.*, 54, 2373-2386.

Fu, X., B. Wang, T. Li, and J.P. McCreary (2003). Coupling between northward-propagating, intraseasonal oscillations and sea surface temperature in the Indian Ocean. *J. Atmos. Sci.*, 60, 1733-1753.

Gaspar, P., Y. Grégoris, and J.-M. Lefevre (1990). A simple eddy kinetic energy model for simulations of the oceanic vertical mixing: Tests at station Papa and long-term upper ocean study site. *J. Geophys. Res.*, 95(C9), 16179-16193.

Gentemann, C. L., C. J. Donlon, A. Stuart-Menteth, and F. J. Wentz (2003). Diurnal signals in satellite sea surface temperature measurements. *Geophys. Res. Lett.*, 30, 1140, doi:10.1029/2002GL016291.

Gentemann, C. L., P. J. Minnett, and B. Ward (2009). Profiles of ocean surface heating (POSH): A new model of upper ocean diurnal warming. *J. Geophys. Res.*, 114, C07017, doi:10.1029/2008JC004825.

Hendon, H.H., and J. Glick (1997). Intraseasonal air-sea interaction in the tropical Indian and Pacific Oceans. *J. Climate*, 10, 647-661.

Hendon, H.H., B. Liebmann, M. Newman, J.D. Glick, and J.E. Schemm (2000). Medium-range forecast errors associated with active episodes of the Madden-Julian Oscillation. *Mon. Wea. Rev.*, 128, 69-86.

Inness, P.M., and J.M. Slingo (2003). Simulation of the Madden-Julian oscillation in a coupled general circulation model. Part I: Comparison with observations and an atmosphere-only GCM. *J. Climate*, 16, 345-364.

Jerlov, N. G. (1976). *Marine Optics*, 231 pp., Elsevier, New York, 1976.

Jones, C., D.E. Waliser, and C. Gautier (1998). The Influence of the Madden-Julian Oscillation on ocean surface heat fluxes and sea surface temperature. *J. Climate*, 11, 1057-1072.

Jones, C., D. Waliser, K. Lau and W. Stern (2004). The Madden-Julian Oscillation and its impact on Northern Hemisphere weather predictability. *Mon. Wea. Rev.*, 132, 1462–1471.

Kawai, Y., and H. Kawamura (2000). Study on a platform effect in the in situ sea surface temperature observations under weak wind and clear sky conditions using numerical models. *J. Atmos. Oceanic Technol.*, 17, 185-196.

Kawai, Y., and A. Wada (2007). Diurnal sea surface temperature variation and its impact on the atmosphere and ocean: A review. *J. Oceanogr.*, 63, 721–744.

Kim, J.H., C.H. Ho, H.S. Kim, C.H. Sui, and S.K. Park (2008). Systematic variation of summertime tropical cyclone activity in the western North Pacific in relation to the Madden-Julian Oscillation. *J. Climate*, 21, 1171-1191.

Kessler, W.S., and R. Kleeman, (2000). Rectification of the Madden-Julian Oscillation into the ENSO cycle. *J. Climate*, 13, 3560-3575.

Kobayashi, C., S. Maeda, A. Ito, Y. Matsushita and K. Takano (2005). Relation between SSTs and predictability of seasonal mean precipitation over the western tropical Pacific. *J. Meteorol. Soc. Japan*, 83, 919–929.

Kondo, J., Y. Sasano, and T. Ishii (1979). On Wind-Driven Current and Temperature Profiles with Diurnal Period in the Oceanic Planetary Boundary Layer. *J. Phys. Oceanogr.*, 9, 360-372.

Knutson, T. R., and K. M. Weickmann (1987). 30–60 day atmospheric oscillations: Composite life cycles of convection and circulation anomalies. *Mon. Wea. Rev.*, 115, 1407-1436.

Large, W. G., J. C. McWilliams, and S. C. Doney (1994). Oceanic vertical mixing: A review and a model with a nonlocal boundary layer parameterization. *Rev. Geophys.*, 32(4), 363-403.

Lau, K.M., and C. H. Sui (1997). Mechanisms of Short-Term Sea Surface Temperature Regulation: Observations during TOGA COARE. *J. Climate*, 10, 465-472.

Lau, K. M., and P. H. Chan (1986). Aspects of the 40-50 day oscillation during the Northern summer as inferred from outgoing longwave radiation. *Mon. Wea. Rev.*, 114, 1354–1367.

Lebeaupin C. B., V. Ducrocq, H. Giordani (2009). Two-way one-dimensional high-resolution air-sea coupled modelling applied to Mediterranean heavy rain events. *Quart. J. Roy. Meteorol. Soc.*, 135, 187–204.

Leipper DF. (1967). Observed ocean conditions and Hurricane Hilda (1964). *J. Atmos. Sci.*, 24, 182-96.

Liebmann, B., H. H. Hendon and J. D. Glick (1994). The relationship between tropical cyclone of the western Pacific and Indian Oceans and the Madden-Julian Oscillation. *J. Meteor. Soc. Japan*, 72, 401–411.

Liebmann B. and C.A. Smith (1996). Description of a complete (interpolated) outgoing longwave radiation dataset. *Bull. Amer. Meteorol. Soc.*, 77, 1275–1277.

Madden, R. A., and P. R. Julian (1994). Observations of the 40–50 day tropical oscillation: A review. *Mon. Wea. Rev.*, 122, 814–837.

Maloney, E.D., and A.H. Sobel (2004). Surface fluxes and ocean coupling in the tropical intraseasonal oscillation. *J. Climate*, 17, 4368-4386.

Matthews AJ, (2004). The atmospheric response to observed intraseasonal tropical sea surface temperature anomalies. *Geophys. Res. Lett.*, 31 (14), L14107.

Mellor, G. L. (2001). One-dimensional, ocean surface layer modelling: A problem and a solution. *J. Phys. Oceanogr.*, 31, 790-809.

Nakazawa, T. (1986). Intraseasonal variation of OLR in the tropics during the FGGE year. *J. Meteor. Soc. Japan*, 64, 17–34.

Pimentel, S., K. Haines, and N. K. Nichols (2008). The assimilation of satellite-derived sea surface temperatures into a diurnal cycle model. *J. Geophys. Res.*, 113, C09013, doi:10.1029/2007JC004608.

Saha, S., S. Nadiga, C. Thiaw, J. Wang, W. Wang, Q. Zhang, H.M. Van den Dool, H.L. Pan, S. Moorthi, D. Behringer, D. Stokes, M. Peña, S. Lord, G. White, W. Ebisuzaki, P. Peng, and P. Xie (2006). The NCEP Climate Forecast System. *J. Climate*, 19, 3483-3517.

Shinoda, T., and H.H. Hendon (1998). Mixed layer modeling of intraseasonal variability in the tropical western Pacific and Indian Oceans. *J. Climate*, 11, 2668-2685.

Shinoda, T. (2005). Impact of the diurnal cycle of solar radiation on intraseasonal SST variability in the western equatorial Pacific. *J. Climate*, 18, 2628-2636.

Simmons, A., S. Uppala, D. P. Dee and S. Kobayashi (2007). ERA-Interim: New ECMWF reanalysis products from 1989 onwards. *ECMWF Newsletter*, 110, 25–35.

Slingo, J.M., P.M. Inness, R.B. Neale, S.J. Woolnough and G-Y. Yang, (2003). Scale interactions on diurnal to seasonal timescales and their relevance to model systematic errors. *Annals of Geophysics*, 46, 139–155.

Sperber, K.R. (2003). Propagation and the vertical structure of the Madden-Julian Oscillation. *Mon. Wea. Rev.*, 131, 3018-3037.

Sperber, K. R., S. Gualdi, S. Legutke and V. Gayler (2005). The Madden-Julian oscillation in ECHAM4 coupled and uncoupled general circulation models. *Clim. Dyn.*, 25, 117–140.

Stramma, L., P. Cornillon, and J. F. Price (1986). Satellite observations of sea surface cooling by hurricanes. *J. Geophys. Res.*, 91(C4), 50315035.

Takaya, Y., J.-R. Bidlot, A. C. M. Beljaars, P. A. E. M. Janssen (2010). Refinements to a prognostic scheme of skin sea surface temperature. *J. Geophys. Res.*, 115, C06009, doi:10.1029/2009JC005985.

Taylor, P. A. (1989). Comments on: Elimination of spurious inertial oscillations in boundary-layer models with time-dependent geostrophic winds. *Boundary-Layer Meteorology*, 48, 445–446.

Vitart, F. (2009). Impact of the Madden Julian Oscillation on tropical storms and risk of landfall in the ECMWF forecast system. *Geophys. Res. Lett.*, L15802, doi:10.1029/2009GL039089.

Vitart, F. and F. Molteni (2009a). Dynamical extended-range prediction of early monsoon rainfall over India. *Mon. Wea. Rev.*, 137, 1480–1492.

Vitart, F. and F. Molteni (2009b). Simulation of the MJO and its teleconnections in an ensemble of 46-day EPS hindcasts. *ECMWF Technical Memorandum*, 597, pp. 60.

Vitart, F., R. Buizza, M. Alonso Balmaseda, G. Balsamo, J.-R. Bidlot, A. Bonet, M. Fuentes, A. Hofstadler, F. Moleni and T. Palmer (2008). The new VAREPS-monthly forecasting system: A first step towards seamless prediction. *Quart. J. Roy. Meteor. Soc.*, 134, 1789–1799.

Vitart, F., S. J. Woolnough, M. A. Balmaseda and A. M. Tompkins (2007). Monthly forecasting of the Madden-Julian Oscillation using a coupled GCM. *Mon. Wea. Rev.*, 135, 2700–2715.

Wada, A. (2005). Numerical simulations of sea surface cooling by a mixed layer model during the passage of typhoon Rex. *J. Oceanogr.*, 61, 41–57.

Wada, A. (2009). Idealized numerical experiments associated with the intensity and rapid intensification of stationary tropical-cyclone-like vortex and its relation to initial sea-surface temperature and vortex-induced sea-surface cooling. *J. Geophys. Res.*, 114, D18111, doi:10.1029/2009JD011993.

Waliser, D.E., K.M. Lau, and J.H. Kim (1999). The influence of coupled sea surface temperatures on the Madden-Julian Oscillation: A model perturbation experiment. *J. Atmos. Sci.*, 56, 333-358.

Wang, B., Q. Ding, X. Fu, I.-S. Kang, K. Jin, J. Shukla, and F. Doblas-Reyes (2005). Fundamental challenge in simulation and prediction of summer monsoon rainfall. *Geophys. Res. Lett.*, 32, L15711, doi:10.1029/2005GL022734.

Webster, P. J., C. A. Clayson and J. A. Curry (1996). Clouds, radiation and the diurnal cycle of sea surface temperature in the tropical western Pacific Ocean. *J. Climate*, 9, 1712–1730.

Wentz, F. J., C. Gentemann, D. Smith, D. Chelton (2000). Satellite measurements of sea surface temperature through clouds. *Science*, 288, 847–850.

Wheeler, M.C. and H.H. Hendon (2004). An all-season real-time multivariate MJO index: Development of an index for monitoring and prediction. *Mon. Wea. Rev.*, 132, 1917–1932.

Woolnough, S. J., F. Vitart and M. A. Balmaseda (2007). The role of the ocean in the Madden-Julian Oscillation: Implications for MJO prediction. *Quart. J. Roy. Meteor. Soc.*, 133, 117–128.

Yasunari T. (1979). Cloudiness fluctuations associated with the Northern Hemisphere summer monsoon. *J. Met. Soc. Japan*, 57, 227–242.

Zeng, X., and A. Beljaars (2005). A prognostic scheme of sea surface skin temperature for modeling and data assimilation. *Geophys. Res. Lett.*, 32, L14605.

Zeng, X., and R. E. Dickinson (1998). Impact of diurnally-varying skin temperature on surface fluxes over the tropical Pacific. *Geophys. Res. Lett.*, 25(9), 1411-1414.

Zhang, C. (2005). Madden-Julian Oscillation. *Reviews of Geophysics*, 43, 1–36.

Zheng Y., D. E. Waliser, W. F. Stern, C. Jones (2004). The role of coupled sea surface temperatures in the simulation of the tropical intraseasonal oscillation. *J. Climate*, 17, 4109–4134.